Journal Pre-proofs

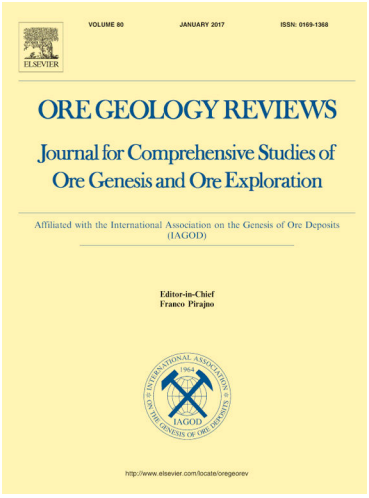

The Pilot Knob Iron Ore Deposits in Southeast Missouri: A High-To-Low Temperature Magmatic-Hydrothermal Continuum

Bolorchimeg N. Tunnell, Marek Locmelis, Cheryl Seeger, Ryan Mathur, István Dunkl, Brandon Sullivan, Lisa Lori

PII: S0169-1368(20)31158-6
DOI: https://doi.org/10.1016/j.oregeorev.2020.103973
Reference: OREGEO 103973

To appear in: *Ore Geology Reviews*

Received Date: 2 September 2020
Revised Date: 15 December 2020
Accepted Date: 30 December 2020

Please cite this article as: B.N. Tunnell, M. Locmelis, C. Seeger, R. Mathur, I. Dunkl, B. Sullivan, L. Lori, The Pilot Knob Iron Ore Deposits in Southeast Missouri: A High-To-Low Temperature Magmatic-Hydrothermal Continuum, *Ore Geology Reviews* (2021), doi: https://doi.org/10.1016/j.oregeorev.2020.103973

The Pilot Knob Iron Ore Deposits in Southeast Missouri: A High-To-Low Temperature Magmatic-Hydrothermal Continuum

Bolorchimeg N. Tunnell[1], Marek Locmelis[1*], Cheryl Seeger[2], Ryan Mathur[3], István Dunkl[4], Brandon Sullivan[1], Lisa Lori[5]

[1] Department of Geosciences and Geological and Petroleum Engineering, Missouri University of Science & Technology, Rolla, Missouri, USA.
[2] Missouri Department of Natural Resources, Missouri Geological Survey
[3] Juniata College, 1700 Moore St, Huntingdon, Pennsylvania 16652, USA
[4] Sedimentology and Environmental Geology, Geoscience Center, University of Göttingen, Germany
[5] Doe Run Company, PO Box 500, Viburnum, Missouri 65566, USA

*corresponding author: Marek Locmelis, locmelism@mst.edu, Missouri University of Science & Technology 1400 N Bishop Avenue, 334 McNutt Hall, Rolla, MO 65409.

Abstract

The Mesoproterozoic St. Francois Mountains igneous terrane in southeast Missouri contains eight major and several minor IOA/IOCG-type deposits. This study focuses on the Pilot Knob deposits, i.e., the largely massive Pilot Knob Magnetite (PKM) deposit and the Pilot Knob Hematite (PKH) deposit, which is located 240 m stratigraphically above the PKM and consists of variably mineralized bedded hematite and ore hosted in brecciated volcanic agglomerates. The PKM deposit was previously shown to be of magmatic and magmatic-hydrothermal origin, although its formation has not been precisely dated. The origin of the PKH deposit (i.e., sedimentary vs. hydrothermal) and its genetic relationship to the PKM, remain controversial.

We present new U-Pb data on apatite intergrown with massive magnetite in the PKM deposit and provide the first precise age for the formation of the PKM ore at 1437.7±5.8 Ma. Petrographic observations of PKH ore, bulk rock compositions, and the mineral chemistry of hematite, which contains up to 2.7% Ti, suggest that the hematite in the PKH deposit crystallized from acidic and hypersaline hydrothermal fluids at a temperature between 200–250°C. The Fe isotopic composition of 9 bedded (δ^{56}Fe = 0.05-0.30‰, average 0.13‰) and 3 brecciated hematite samples (δ^{56}Fe = -0.19-0.01‰, average -0.06‰) from the PKH deposit are slightly lighter than the published δ^{56}Fe results of magnetite from the PKM deposit (δ^{56}Fe = 0.06-0.27‰,

average 0.17‰). However, all isotopic signatures fall within the magmatic range, indicating that iron in both deposits was originally sourced from a magma. Because of the hydrothermal origin of the PKH deposit, the iron isotopic compositions of the PKM and PKH ores that imply a shared/similar iron source, and the spatial proximity of both deposits, we argue that the PKM and PKH deposits are genetically related and represent two endmembers of a high-to-low temperature magmatic-hydrothermal continuum. In this scenario, ore fluids exsolved from the magma that facilitated the formation of the PKM deposit migrated upwards, infiltrated existing sedimentary structures near the surface, and precipitated hydrothermal hematite ore while preserving the original bedded and brecciated structures.

Geochemical signatures of the rhyolites/rhyodacites that host the PKM deposit imply that these rocks are A2-type felsic rocks that were emplaced in a post-collisional extensional setting. Bulk silicate Earth normalized patterns of the PKM deposit and wall rocks display a negative slope from Cs to Lu with negative Nb and Ta anomalies, indicating a hydrous source for the rhyolites and rhyodacites, possibly a subduction-modified subcontinental lithospheric mantle (SCLM). These geochemical signatures support a proposed tectonic setting of the St. Francois Mountains, wherein the igneous terrane developed on a growing continental margin. Episodic mafic-to-intermediate magmatism, and subsequently exsolved hydrothermal fluids, may have formed the cluster of IOA/IOCG-type deposits in the igneous terrane between ~1500 and ~1440 Ma. Within such a context, the PKM and PKH deposits may represent a shallow, small-scale snapshot of processes similar to the ones that form the IOA-IOCG continuum: a deeper magmatic event that exsolved a hydrothermal fluid that forms an overlying ore body.

Keywords: Southeast Missouri, IOA/IOCG deposits, Sedimentary iron formation, Iron isotopes, critical minerals, Apatite U-Pb geochronology

1. Introduction

The southeast Missouri (USA) Iron Metallogenic Province hosts eight major and over thirty minor iron ore deposits or prospects (Kisvarsanyi and Proctor, 1967). These deposits are spatially associated with 1.50 to 1.44 Ga granites and rhyolites of the St. Francois Mountains terrane, which is part of the broader Mesoproterozoic Eastern Granite-Rhyolite terrane that developed along the southern margin of Laurentia (Fig. 1; Bickford and Mose, 1975; Kisvarsanyi, 1981; Kisvarsanyi, 1990; Van Schmus et al., 1996; Bickford et al., 2015; Day et al.,

2016; Watts and Mercer, 2020). Near-surface magnetite and hematite iron oxide deposits such as the Iron Mountain, Shepherd Mountain, Pilot Knob Hematite, and Cedar Hill deposits have been discovered and exploited since the early 1800s, with over 100 million tonnes produced (Seeger, 2000; Starkey and Seeger, 2016). Aeromagnetic surveys of southeast Missouri in the 1940s led to the discovery of large subsurface deposits including Pea Ridge, Bourbon, Kratz Spring, Camels Hump, Boss, and the Pilot Knob Magnetite deposits (Seeger, 2000). Although iron ore reserves in southeast Missouri are estimated at nearly 1 billion tonnes (Arundale and Martin, 1970) and may contain significant critical mineral resources such as rare earth elements (Day et al., 2016), so far only the Pea Ridge and Pilot Knob Magnetite deposits were developed into underground mining operations from 1964 to 2001 and from 1968 to 1980, respectively (Starkey and Seeger, 2016).

The iron ore deposits in southeast Missouri have been divided into 4 different types based on the mode of occurrence and metal endowment: (1) Volcanic-hosted iron oxide deposits of magmatic and/or magmatic-hydrothermal origin and similar to "Kiruna-type" deposits; examples include the Pilot Knob Magnetite, Iron Mountain, Pea Ridge, and Kratz Spring deposits (Sidder et al., 1993; Dudley, 1998; Day et al., 2001; Nold et al., 2013); (2) Iron oxide-copper-gold (IOCG) deposits such as at Boss, and potentially Bourbon and Camels Hump (Kisvarsanyi and Smith, 1988; Brandom, 1989; Day et al., 2001; Stallings et al., 2001; Seeger, 2003); (3) Steeply dipping, vein-hosted hydrothermal iron oxide deposits that include the Shepherd Mountain, Shut-Ins, and Hogan deposits (Dudley and Nold, 2001; Dudley and Nold, 2003b; Nold et al., 2014); and (4) Sedimentary hematite iron formations that have been proposed to have originated from exhalations of hydrothermal fluids into caldera lakes, including the Pilot Knob Hematite, Cedar Hill, College Hill, Cuthbertson Mountain, and Russell Mountain deposits (Dudley and Nold, 2003a; 2004; Nold et al., 2014).

This study investigates the genetic relationship between the two iron deposits at Pilot Knob, i.e., the Pilot Knob Magnetite (PKM) deposit and the overlying Pilot Knob Hematite (PKH) deposit (Fig. 2). The PKM deposit is a magnetite-dominated subsurface deposit overlain by 120 m of Cambrian sedimentary rocks. The PKM deposit has previously been suggested to be of magmatic-hydrothermal origin based on textural evidence and magnetite chemistry (Nold et al., 2013), and Fe-O paired isotopic studies of magnetite (Childress et al., 2016). The formation age of the PKM deposit has been inferred to be slightly younger than the host volcanic rocks

based on structural relationships (Day et al., 2016). A younger age limit of 1333±56 Ma for the formation of the PKM deposit was presented by Lowell and Rämö (1999) who dated a dike crosscutting the deposit using bulk rock Sm-Nd geochronology.

The PKH deposit is located 240 m stratigraphically above the PKM ore body and crops out on top of the Pilot Knob Mountain (Fig. 2; Wracher, 1976; Panno and Hood, 1983). In contrast to the PKM deposit, the origin of the PKH deposit and its relationship to the underlying PKM deposit in terms of ore-forming processes continues to be debated. Two distinct mechanisms for the formation of the PKH deposit were previously proposed: (1) Sedimentary iron ore formation in a shallow caldera lake where Fe-bearing hydrothermal fluids vented into the lake and precipitated hematite from the water column (Anderson, 1976; Dudley and Nold, 2004; Nold et al., 2014) and (2) Hydrothermal replacement of volcanoclastic rocks (Kisvarsanyi and Proctor, 1967; Ryan, 1981; Panno and Hood, 1983).

To better constrain the origin of the PKH deposit, we present new petrographic, petrological, and mineralogical observations and integrate these with new bulk rock data (ore and host rock) and compositional and Fe isotopic data of hematite. To assess if an ore genetic relationship exists between the PKH and PKM deposits, we integrate the PKH data with new and published bulk rock and magnetite data (mineral chemistry and Fe isotopes). We further present the first direct age for the formation of the PKM deposit based on U-Pb dating of apatite and interpret the data with regards to ore-forming process in the SE Missouri between 1.5 and 1.4 Ga.

2. Geological setting

The iron oxide deposits in southeast Missouri occur within early Mesoproterozoic (1.50-1.44 Ga) volcanic and volcanoclastic sedimentary rocks that are part of the Precambrian basement (Fig. 1) (Nold et al., 2014; Day et al., 2016). Because the majority of the Precambrian basement is unconformably overlain by several hundred meters of Paleozoic marine sedimentary rocks (Van Schmus et al., 1996), the geological setting of the basement rocks has been largely constrained by the integration of geophysical studies (Kisvarsanyi, 1984) with studies of outcrops near the St. Francois Mountains (Pratt et al., 1979; Bickford et al., 1981) and drill core studies (Kisvarsanyi, 1980; 1981). The integrated studies show that the basement rocks are predominantly comprised of three terranes, the metasedimentary and metavolcanic Central Plains

orogenic terrane (1.78-1.63 Ga; Sims and Petermar, 1986; Day et al., 2016), and the 1.50-1.30 Ga Eastern and Southern Granite-Rhyolite terranes, both composed of anorogenic granites and associated rhyolites with lesser amounts of basalt and intermediate-composition suites (Bickford et al., 2015; Day et al., 2016). These studies also identified four main caldera structures through which effusive volcanism occurred, i.e., Taum Sauk, Butler Hill, Lake Killarney, and Hawn State Park (Fig. 1; Sides et al., 1981; Day et al., 2016).

The Eastern Granite-Rhyolite (EGR) terrane is the best-studied terrane because it is exposed over 900 km^2 region in the St. Francois Mountains of Missouri. The EGR is predominantly composed of granitic and rhyolitic rocks, with lesser amounts of intermediate-composition rocks and minor basaltic rocks (Ayuso et al., 2016; Day et al., 2016) that were emplaced during two episodes of igneous activity at ~1.50 to 1.44 and ~1.33 to 1.30 Ga (Sides et al., 1981; Kisvarsanyi, 1990; Van Schmus et al., 1996; Thomas et al., 2012; Bickford et al., 2015). Volcanic rocks in the EGR include predominantly porphyritic dacitic and rhyolitic ash-flow and air-fall tuffs with eutaxitic and fiamme textures, abundant quartz and alkali feldspar phenocrysts, and intermediate-composition flows intercalated with rhyolites and minor basalt dikes (Day et al., 2016). Granitic rocks, overlain by co-magmatic felsic volcanic rocks, occur in three distinct compositions and modes of occurrence, i.e., subvolcanic granite massifs, ring plutons of early Mesoproterozoic age, and central (resurgent) plutons of middle Mesoproterozoic age (Fig. 1) (Kisvarsanyi, 1980; Menuge et al., 2002). Locally, minor late-stage mafic intrusive rocks cut through the felsic intrusive rocks (Kisvarsanyi, 1981). The subvolcanic granite massifs include porphyritic, biotite-alkali feldspar granites that are granophyric near contacts with rhyolite, and grade into equigranular and coarse-grained rapakivi textured varieties at depth (Kisvarsanyi, 1981; Kisvarsanyi, 1990). The ring plutons are composed of granophyric, medium-grained, equigranular, and porphyritic textured amphibole granite, biotite granite, biotite-hornblende granite, biotite-hornblende quartz monzonite, and syenite. The emplacement of these rocks was mostly controlled by ring fractures associated with caldera collapse (Cullers et al., 1981; Kisvarsanyi and Kisvarsanyi, 1990). The central (resurgent) plutons are largely composed of two-mica granite (muscovite-biotite) and contain a distinctive suite of accessory minerals including fluorite, topaz, apatite, spinel, allanite, monazite, titanite, zircon, garnet, and cassiterite (Kisvarsanyi and Kisvarsanyi, 1990). The central plutons display distinctively low magnetic anomalies in circular to oval shape and are regarded as Graniteville-type granites (Kisvarsanyi,

1984; Kisvarsanyi and Kisvarsanyi, 1989; McCafferty et al., 2016). Geochemical and radiogenic isotopic (Sr, Nd, Pb) studies on the basement granitoids suggest that the EGR terrane developed from juvenile magma with minimal crustal contamination (Menuge et al., 2002; Walker et al., 2002; Ayuso et al., 2016; Day et al., 2016).

2.1 Geology of the Pilot Knob Magnetite deposit

The Pilot Knob Magnetite deposit is located in Iron County, Missouri, and produced 20 Mt of iron ore during its underground operation (Ryan, 1981). The PKM deposit consists of a series of tabular, sill-like bodies that strike northwest and dip to the southwest at approximately 45°, and are concordant to layering within the host sequence of pink to gray rhyolitic pyroclastic rocks (Wracher, 1976; Panno and Hood, 1983; Nold et al., 2013). The approximate dimensions of the deposit are 500 m (strike) x 700 m with a 45° downdip and a thickness of 100 m (Nold et al., 2013). The mineralization is dominated by relatively homogeneous higher-grade, black granular magnetite ore that forms the bulk of the orebody, and a lower-grade, relatively heterogeneous magnetite ore that envelops the higher-grade ore (Nold et al., 2013). The upper part of the orebody was exposed on the Precambrian unconformity, partially altered to hematite, and is unconformably overlain by the Upper Cambrian Lamotte Sandstone (Nold et al., 2013). The deposit is crosscut by the 125 m thick near-horizontal Shepherd Mountain Gabbro at a depth of 500 m. The Shepherd Mountain Gabbro was dated at 1333±56 Ma using bulk rock Sm-Nd geochronology (Lowell and Rämö, 1999); this age has been interpreted to represent the younger age limit of ore body emplacement (Nold et al., 2013). The style of deformation in the deposit is brittle fracturing and brecciation, with no penetrative structural fabrics observed (Day et al., 2016).

2.2 Geology of the Pilot Knob Hematite deposit

The Pilot Knob Hematite surface deposit (Fig. 2A) is located 1000 meters east of the town of Pilot Knob and produced 1.6 Mt of iron ore from 1847 until mining ceased in 1890 (Crane, 1912; Panno and Hood, 1983). The Pilot Knob mountain itself is a cone-shaped hill composed of a series of volcanic rocks. The stratigraphic units from the crest of the mountain to the top are the ‘lower red rhyolite’, the ‘purple rhyolite’, a series of ore beds, a volcanic agglomerate unit, and the ‘upper red rhyolite’ (Fig. 2B; Panno and Hood, 1983). The volcanic

units are folded and form a shallow syncline that plunges ~20° to the southwest (Ryan, 1981; Panno and Hood, 1983). The hematite orebody (Fig. 2C) is composed of a series of laminated hematite ore beds (4.8 to 18 m in thickness) and overlain by an up to 30-m-thick volcanic agglomerate unit that contains fine-grained siliceous hematite in a matrix (Ryan, 1981; Seeger et al., 1989). The laminated ore beds are divided into the lower and upper ore beds that are separated by an up to 1 m thick clay seam (Ryan, 1981). The lower ore bed, which occurs underground with some blocks being accessible at the surface due to mine workings (Fig. 3A, B), is dominated by fine-grained, hard, dense, steel-gray, thinly laminated specular hematite with an average ore grade of 58% Fe (Ryan, 1981; Seeger et al., 1989). The lower ore bed contains no to very few clasts and is characterized by ripple marks and raindrop or possibly ash fall prints in its lower portion (Ryan, 1981; Seeger et al., 1989). The thickness of each lamina varies from 2.5 mm up to 2.5 cm (Seeger et al., 1989). The upper ore bed occurs above ground with strike between 200-220° and dipping angle between 21-25° and is also composed of thinly laminated, fine-grained, bluish-gray hematite with an Fe ore grade between 40 and 50% (Ryan, 1981; Seeger et al., 1989). Similar to the lower ore bed, the upper ore bed also contains ripple marks and mudcracks (Seeger et al., 1989). The upper ore bed is characterized by alternating red and dark laminas that vary between 2 mm and 3 cm in thickness and contain minor clay bands of 0.1-0.5 cm thickness (Seeger et al., 1989). The lower portion of the upper ore bed contains sparse rhyolitic clasts with sizes of 0.5-2 cm and thin uniform bands (up to 15 cm thick) consisting of quartz and feldspar phenocrysts parallel to the bedding (Seeger et al., 1989). With increasing stratigraphic height, the size (up to 15 cm in the longest direction) and abundance (up to 25 modal %) of rhyolite clasts increase (Seeger et al., 1989). The volcanic agglomerate that overlies the bedded units contains angular to sub-rounded fragments of rhyolite porphyry with up to 30 cm in the longest direction and fine-grained siliceous hematite in the matrix with an iron ore grade of 20-23% (Seeger et al., 1989). Some fragments are laid with their longest dimensions parallel to the bedding (Ryan, 1981). It is noted that the number of clasts and their size in the agglomerate increase with stratigraphic height (Ryan, 1981; Seeger et al., 1989). No structural overprinting resulting in a penetrative planar fabric such as cleavage or schistosity are present, implying that the stratigraphic section was never deeply buried nor had experienced regional metamorphism (Day et al., 2016).

3. Methods

3.1 Sample preparation

Twenty-two hematite-mineralized samples from the PKH deposit were collected from still accessible surface outcrops, mine workings, or unprocessed ore material at the surface (Fig. 3A-F). For the subsurface PKM deposit, 14 drill core samples (Fig. 3G-J) were retrieved from the McCracken Core Repository of Missouri Department of Natural Resources. A list of samples including location and mode of sampling is presented in Table 1. All samples were prepared as polished one-inch diameter mounts. Five samples from the PKH were also prepared as thin sections.

Ultra-pure mineral concentrates (30-50 mg) for iron isotope analysis were prepared from twelve PKH samples (hematite) and one PKM sample (magnetite) in the Department of Geosciences and Geological and Petroleum Engineering (GGPE) at Missouri University of Science and Technology (Missouri S&T). The samples were crushed using an agate mortar and pestle and cleaned using ultrasonic distilled water baths. The samples were then dry-sieved to a grain size of 75 to 150 μm. Magnetite from the PKM sample was separated into magnetic and nonmagnetic fractions using a hand magnet. Hematite and magnetite from all samples were hand-picked under a Leica binocular microscope to produce the ultra-pure mineral concentrates.

3.2 Petrographic studies

The samples were studied using reflected- and transmitted-light microscopy using a Leica DVM 6 digital microscope at Missouri S&T. A subset of samples was further characterized using a Hitachi S4700 scanning electron microscope located in the Advanced Materials Characterization Laboratory (AMCL) at Missouri S&T and back-scattered electron imaging using a JEOL JXA-8200 electron microprobe in the Department of Earth and Planetary Sciences, Washington University, St. Louis, Missouri, USA.

3.3 Electron microprobe analysis

The major and minor element chemistry of magnetite and hematite was determined using a JEOL JXA-8200 electron microprobe equipped with wavelength and energy dispersive spectrometers (WDS and EDS) at Washington University. The analyses were conducted in WDS

mode using a 5 µm diameter beam with an accelerating voltage of 15 kV and a beam current of 50 nA. Calibration and data reduction were done with measurements on natural and synthetic standard materials. Typical detection limits were 90 ppm for K and Ca, 100 ppm for Cr and V, 120 ppm for Mg, Al, and Ti, 140 ppm for Si and Mn, 230 ppm for Na, Co, and Ni, and 420 ppm for Zn. Repeated analyses of the standards show that major elements were determined with an accuracy of ≤3% and an external precision of ≤3% (2-sigma), whereas minor elements were determined with an accuracy of ≤5% and an external precision of ≤4% (2-sigma). Average electron microprobe analysis for different mineralization styles are presented in Table 2; all data are provided as electronic appendix (A-1).

3.4 Iron isotope analysis

Ultra-pure magnetite and hematite concentrates were dissolved in 4 ml heated ultrapure aqua regia and the solutions were dried. Iron was purified using a BioRad MP-1 anion exchange resin after drying the Fe solution using the protocol by Maréchal et al. (1999). The iron isotopic composition was then measured using a Neptune multi-collector (MC)-ICP-MS at Pennsylvania State University. The instrument setup, sample introduction, and running conditions used are described in Yesavage et al. (2016). The analysis was conducted in high-resolution mode and samples were measured at approximately 3 ppm, which generated a 15V signal on the shoulder of the Fe peak. Mass bias was corrected for by using standard-sample-standard bracketing. Results are presented in the traditional per mil format with Fe isotope values compared to international IRMM-014 standard (Institute for Reference Materials and Measurements, Belgium, Taylor et al., 1992). The in-house and international standards SRM-3126a (Yesavage et al., 2016) and HPS-WU (Beard et al., 2003) with accepted values of $\delta^{56}Fe = 0.34‰ \pm 0.1‰$ 2σ and $\delta^{56}Fe = 0.60‰ \pm 0.07‰$ 2σ, respectively, were used to assess the accuracy and precision of the analyses; all errors fall within the range of 0.1‰ 2σ of the standards. Values reported in Table 3 are an average of two different measurements.

3.5 Apatite U-Pb geochronology

In-situ U-Pb dating of apatite was performed in the Geoscience Center at the University of Göttingen, Germany, using a RESOLution S-155 (Resonetics) 193 nm excimer laser ablation (LA) system (CompexPro 102) connected to a ThermoScientific Element 2 sector field (SF) ICP-

MS equipped with a two-volume ablation cell (Laurin Technic). The method employed for the analysis is described by Ring and Gerdes (2016) and Chew et al. (2011). All age data were obtained by single spot analyses with a laser beam diameter of 33 μm. The laser was fired at a repetition rate of 5 Hz and at nominal laser energy output of 25%. Two laser pulses were used for pre-ablation. Helium and Ar were used as carrier gases. Analytes of ^{238}U, ^{235}U, ^{232}Th, ^{208}Pb, ^{207}Pb, ^{206}Pb, mass204, and ^{202}Hg were measured. The data reduction is based on the processing of ca. 46 selected time slices (corresponding to ca. 13 seconds) starting ca. 3 sec. after the beginning of the signal. If the ablation hit zones or inclusions with highly variable actinide concentrations or isotope ratios, then the integration interval was resized or the analysis was discarded. The individual time slices were tested for possible outliers by an iterative Grubbs test applied at the P=5% level. This test filtered out only extremely biased time slices and usually less than 2% of the time slices were rejected.

The mass bias, inter-element fractionation, drift over the sequence time and the down-hole fractionation were controlled and corrected by bracketing the unknown samples using NIST614 and 612 soda-lime glasses and the GJ-1 zircon reference material (Jackson et al., 2004). The Madagascar apatite reference material was used to correct the effect of the non-silicate matrix of the dated phases (Thomson et al., 2012). The Durango, McClure Mountain and 401 reference apatites were employed as secondary age standards and treated as unknowns during analysis (McDowell et al., 2005; Schoene and Bowring, 2006).

Drift- and fractionation corrections and data reductions were performed using UranOS (Dunkl et al., 2008). Data were plotted in the Tera-Wasserburg diagram and the ages were calculated as lower intercepts using Isoplot 3.75 (Ludwig, 2012) and IsoplotR (Vermeesch, 2018). All uncertainties are reported at the 2-sigma level.

3.6 Bulk rock geochemical analysis

The major, minor, and trace elements bulk rock geochemistry of host volcanic rocks of the PKM deposit and magnetite and hematite ores from the PKM and PKH deposits was determined using X-Ray Fluorescence (XRF) and inductively coupled plasma-mass spectrometry (ICP-MS), following open vessel multi-acid digestion at Activation Laboratories (Ontario, Canada). Major and minor elements were determined with typically better than 6% and a 2-

sigma external precision ≤3%, whereas most trace elements were determined with an accuracy of ≤10% and a precision of ≤9% (2-sigma).

4. Results

4.1 Ore petrography of the PKM and PKH deposits

4.1.1 Ore petrography of the PKM deposit

Samples from the PKM deposit display a range of ore textures from massive to matrix and disseminated magnetite ore with minor amounts of hematite, rutile and traces of pyrite, molybdenite, and ilmenite (Fig. 4). Most samples with matrix and massive magnetite are hematite free. However, in samples where minor hematite does exist, it replaces hematite showing a caries texture (Fig. 4A, B); additionally, minor martite is observed that formed from magnetite alteration. Disseminated magnetite is commonly euhedral to subhedral with sizes varying from a few microns to up to 1 mm (Fig. 4C, D). Samples from shallow depth (Sample ID: PKM-1098-580; depth of 176.8 m in drill core) contain abundant disseminated anhedral hematite with sizes between a few microns and 400 μm in the longest direction and show abundant martitization of magnetite along the edges of grains (Fig. 4D). Some magnetite grains contain barite and ilmenite inclusions (Fig. 4E) while others are locally intergrown or in contact with apatite with sizes between 10 μm and 100 μm (Fig. 4F).

4.1.2 Ore petrography of the PKH deposit

The hematite ore samples from the PKH deposit show bedded and brecciated textures. *Bedded hematite:* The bedded hematite samples are composed of hematite (up to 70%), quartz and sericite (Fig. 5, 6). Both primary and secondary quartz are found in the samples. Primary quartz grains display euhedral to anhedral textures with grain sizes varying from a few microns to 600 μm in the longest direction (Fig. 5A, 6C). The primary quartz lacks evidence of structural overprinting. Secondary quartz often shows a mosaic texture (Fig. 5B, D, F). Some primary quartz grains are overgrown with secondary mosaic quartz (Fig. 5D). Sericite occurs interstitially between quartz and hematite or within mosaic-textured quartz (Fig. 5B, C, E, F). Hematite occurs as primary single and aggregated crystals in bedded samples from the PKH (Fig. 6), not showing any textural or compositional evidence for a secondary formation via replacement.

Hematite aggregates and single specular hematite grains vary in size from a few microns to 300 μm in the longest direction and are randomly oriented.

Brecciated hematite: Hematite in brecciated samples occurs as primary single and aggregated crystals in both fragments and surrounding matrix (Fig. 7). The sizes for hematite aggregates and single hematite grains vary from a few microns to 400 μm in the longest direction. A few hematite aggregates in brecciated samples contain trace amounts of ilmenite and pyrite inclusions (Fig. 7C, E, F). Minor hematite aggregates within brecciated samples display random or trellis-sandwich type ilmenite exsolution (Fig. 7C, F) and are interpreted to be secondary as discussed below.

4.2 Oxide mineral chemistry

4.2.1 Oxide mineral chemistry of the PKM deposit

Minor and trace elements contents of magnetite and hematite are summarized in Figure 8A and Table 2. A total of 143 magnetite and 29 hematite measurements were carried out on 6 samples from the PKM deposit (Fig. 8A, Table 2, Appendix A-1). Magnetite shows variable contents of Mn (160 – 10,300 ppm, average of 950 ppm), Ti (140 – 8,500 ppm, average of 1,600 ppm), and V (110 – 410 ppm, average of 280 ppm). However, 17% of the analyses did not yield Ti above the lower level of detection (120 ppm), and 41% of the analyses did not detect V (lower level of detection of 100 ppm), likely reflecting analytical limitations of electron microprobe analysis at trace element levels rather than two distinct magnetite populations (i.e., Ti and V bearing vs. Ti and V free). Several grains also contained measurable amounts of Na, Mg, Al, Si, K, Ni, Cr, Ca, and Zn (Fig. 8A, Table 2, Appendix A-1).

Hematite grains generally contain between 140 – 45,000 ppm of Ti (average of 7,400 ppm), 120 – 380 ppm of V (average of 210 ppm), and 140 – 500 ppm of Mn (average of 290 ppm). Only 45% of the analyses detected V (detection limit of 100 ppm), and only 41% yielded Mn concentrations above the detection limit (140 ppm). Similar to the observations made for Ti and V in magnetite, we interpret the analyses below the detection limit to reflect the analytical limitations of the electron microprobe analysis at trace element levels rather than the presence of two different hematite populations. Several grains also contain measurable amounts of Mg, Al, Si, K, Ni, Ca, and Zn (Fig. 8A, Table 2, Appendix A-1).

4.2.2 Oxide mineral chemistry of the PKH deposit

Minor and trace element contents of hematite are summarized in Figure 8B and Table 2. A total of 101 hematite analyses were carried out on 7 bedded samples, while 96 analyses were carried out on hematite from 5 brecciated samples. In the bedded samples, hematite contains between 180 – 26,000 ppm of Ti (average of 3,800 ppm), although 19% of the analyses did not yield Ti above the lower level of detection of 120 ppm. Aluminum is detected in 48% of the analyses with concentrations between 125 – 12,000 ppm (average of 800 ppm; detection limit of 120 ppm). Silica was found in 42% of the grains with contents between 220 – 13,000 ppm (average of 2,200 ppm, detection limit of 140 ppm). We interpret the analyses below the detection limit to reflect limitations of electron microprobe analysis at low concentrations rather than the presence of distinct hematite populations. Several grains also contain trace amounts of Na, Mg, Mn, K, Ni, Cr, Ca, Zn, and V (Fig. 8B, Table 2, Appendix A-1).

Hematite grains in brecciated samples are divided into primary and secondary phases based on the absence (primary) or presence (secondary) of ilmenite exsolutions. Primary hematite grains (i.e., without ilmenite exsolutions) contain between 120 – 17,000 ppm of Ti (average of 4,000 ppm, detection limit 120 ppm) in 69% of the analyses. Approximately 50 % of the analyses also detected notable amounts of Al (120 – 6,300 ppm Al, average of 870 ppm, detection limit 120 ppm). Several grains also contain trace amounts of Na, Mg, Si, Mn, K, Ni, Cr, Ca, Zn, and V (Fig 8B, Table 2). Secondary hematite grains (i.e., with ilmenite exsolutions) contain between 2400 – 450,000 ppm Ti (average of 96,500 ppm). Aluminum was detected in 88% of the analyses with concentrations between 130 – 4,100 ppm (average of 960 ppm). Approximately 50% of the analyses also detected Cr with concentrations between 100 – 580 ppm (average of 220 ppm). Several grains also contain trace amounts of Na, Mg, Si, Mn, K, Ni, Ca, Zn, and V (Fig. 8B, Table 2, Appendix A-1).

4.3 Stable Fe isotope analysis

The stable Fe isotope compositions of one magnetite sample from the PKM and 12 hematite samples (9 bedded and 3 brecciated) from the PKH are presented in Table 3 and Figure 9 in delta notation relative to IRMM-14 as follows:

$$\delta^{5\#}\text{Fe (‰)} = [(^{5\#}\text{Fe}/^{54}\text{Fe})_{\text{sample}} /(^{5\#}\text{Fe}/^{54}\text{Fe})_{\text{IRMM-014}} - 1] * 1000 \quad (1)$$

where # refers to 6 or 7, depending on the measured mass. The $\delta^{56}Fe$ value of magnetite from the PKM (sample ID: PKM-1160-2105) is 0.13‰, which falls within the range of values between 0.06‰ and 0.27‰, previously reported by Childress et al. (2016) for 6 samples from the PKM deposit with an overall average value of 0.17‰. The $\delta^{56}Fe$ values of bedded hematite aggregate separates from the PKH range between 0.05‰ and 0.30‰ with an average value of 0.13‰ while the $\delta^{56}Fe$ values of brecciated hematite from the volcanic agglomerate range from -0.19‰ to 0.01‰ with an average of -0.06‰.

4.4 Apatite U-Pb geochronology of the PKM deposit

The in-situ apatite U-Pb geochronological analyses were carried out on 58 laser ablation spots. The uranium and thorium concentrations are 6±3 ppm and 12±10 ppm, respectively. Six analyses were rejected due to their high uncertainties. The results of the remaining 52 analyses are summarized in Appendix A-2 and illustrated in Figure 10 using the Tera-Wasserburg plot. The lower intercept age is calculated by the consideration of an anchor common lead composition of 0.95 (Stacey and Kramers, 1975). The matrix-corrected lower intercept age of 1437.7±5.8 Ma can be considered as crystallization age of the apatite.

4.5 Bulk rock geochemistry

New bulk rock data of the host volcanic rocks of the PKM deposit and magnetite- and hematite-mineralized samples from the PKM and PKH deposits collected during this study are integrated with publicly available USGS trace element data of host rock samples of the PKM deposit (sample IDs: PKM-1145-1003.5, PKM-1145-828, PKM-1145-861, PKM-1145, PKM-1145-908.6) as well as magnetite-mineralized samples (sample IDs: PKM-1145-826.9, PKM-1098-462, PKM-1145-954, PKM-1160-2040, PKM-1165-2013; *cf.* compilation by Day et al. (2017)). New bulk rock data collected during this study are presented in Appendix A-3.

The host rocks of the magnetite mineralization of the PKM deposit are defined as rhyolite and rhyodacite on a plot of Nb/Y vs. Zr/Ti using immobile element ratios (Fig. 11A). On a tectonic discrimination diagram, host rhyolite and rhyodacite plot in WPG and VAG+syn-COLG fields (Fig. 11B). These rocks are classified as A-type granite (i.e., anorogenic and generated in a rift setting; Fig 11C) and, more specifically, A2 type granite (generated at a convergent boundary; Fig. 11D).

The host rhyolites and rhyodacites of the PKM deposit display great fractionation from light rare earth elements (LREE) to medium rare earth elements (MREE), but only minor fractionation from MREE to heavy rare earth element (HREE) with a slightly negative Eu anomaly (Fig. 12A, B). This is reflected as $Eu_n/Eu^* = 0.6 – 0.9$ and $(La/Yb)_n = 1.3 – 33.5$, $(Dy/Yb)_n = 0.7 – 1.1$, in binary diagrams (Fig. 12C, D). Magnetite-mineralized samples show a similar pattern, albeit with a wider range of REE values where $(La/Yb)_n = 1.7 – 55.7$ and $(Dy/Yb)_n = 0.3 – 1.2$ (Fig. 12A, C, D). In contrast, hematite-mineralized samples show more restricted variations of REE with a downward concave shape (Fig. 12A) and a more pronounced increase in HREE reflected as $(La/Yb)_n = 25.1 – 233.2$ and $(Dy/Yb)_n = 0.4 – 1$ (Fig. 12D) when compared to magnetite-mineralized samples and the host rocks. Magnetite-bearing samples show no Eu anomalies ($Eu_n/Eu^* = 0.7 – 1.3$), whereas hematite-mineralized samples display a positive Eu anomaly ($Eu_n/Eu^* = 1.2 – 4.8$; Fig. 12C). In the bulk silicate Earth normalized trace element spidergram, all groups of samples display an overall negative slope from Cs to Lu with a negative trough in terms of Nb and Ta, and positive peaks of Ba, U, La, and Pb (Fig. 12B). Host rhyolitic rocks and magnetite-mineralized samples show strong depletion in Sr while some hematite-bearing samples from the PKH contain elevated concentrations of Ba and Sr (Fig. 12B). Both magnetite and hematite-bearing samples show Y negative anomalies while the host rocks display either slightly positive or no anomalies (Fig. 12B).

Fluid-mobile elements such as As, Mo, Sb, and W are plotted against Fe_2O_3 content for the PKM and PKH deposits (Fig. 13). Hematite ore samples from the PKH deposit are more enriched in As, Mo, Sb, and W compared to that of the PKM deposit and these elements show positive correlation with total Fe oxide for the PKH deposit, while the concentrations of these elements are lower in the PKM deposit.

5. Discussion

Iron oxide deposits in southeast Missouri are spatially associated with the early Mesoproterozoic 1.50-1.44 Ga ring complexes of the EGR terrane, and have been inferred to be genetically associated with these rocks (Kisvarsanyi and Proctor, 1967; Kisvarsanyi and Kisvarsanyi, 1989; Nold et al., 2014; Day et al., 2016). Based on magnetite geochemistry (Nold et al., 2013) and magnetite Fe-O paired isotope chemistry (Childress et al., 2016), the PKM deposit has previously been proposed to be of magmatic and magmatic-hydrothermal origin.

However, previous studies did not precisely constrain the mineralization age but instead inferred an age range of 1470 – 1330 Ma based on the emplacement age of the nearby Shepherd Mountain rhyolite (1470±30 Ma; Van Schmus et al., 1996; Bickford et al., 2015) and a gabbroic dike that crosscuts the deposit (1333±56 Ma; Lowell and Rämö, 1999). In contrast to the PKM deposit, the origin of the overlying PKH deposit and its relationship to the PKM deposit in terms of ore-forming processes remain to be fully developed. Here we integrate the new data presented here with previously published bulk rock geochemical data by the USGS (Day et al., 2017) and Fe isotopic data on magnetite by Childress et al. (2016) to provide new insight into:

(i) The age of the PKM deposit,
(ii) The origin of the PKH deposit,
(iii) A possible genetic link between the PKM and PKH deposits, and
(iv) The regional scale processes that facilitated the formation of these iron ore deposits and, by inference, others in southeast Missouri.

5.1 A new age for the formation of the PKM deposit

Apatite U-Pb geochronology has been broadly used to determine mineralization ages of Fe ore deposits such as the Olympic Dam IOCG-type deposit (Krneta et al., 2017), the Chadormalu Fe deposit in the Bafq district (Heidarian et al., 2018), the Pea Ridge IOA-type deposit in SE Missouri (Aleinikoff et al., 2016; Neymark et al., 2016a), and the Carlin-type Au deposits (Chen et al., 2019). Analysis of apatite from the massive magnetite zone of the PKM deposit (sample ID: PKM-1160-2105) yields a U-Pb age of 1437.7±5.8 Ma (Fig. 10). Because the analyzed apatite grains are intergrown with magnetite (Fig. 4F), it is argued that the magnetite and apatite co-crystallized (*cf.* Chen et al., 2019). Consequently, we argue that the magnetite ore of the PKM deposit formed 1437.7±5.8 Ma, which is well within the previous age estimate of 1470 – 1330 Ma.

5.2 New constraints for the formation of the Pilot Knob Hematite deposit

5.2.1 Insight from petrographic observations

Existing studies on the origin of the PKH are limited to short paragraphs in studies that otherwise focus on the PKM or other deposits in southeast Missouri or the volcanic stratigraphy

of the Pilot Knob mountain (Kisvarsanyi and Proctor, 1967; Panno and Hood, 1983; Seeger, 2000; Nold et al., 2013; Nold et al., 2014), conference proceedings (Dudley and Nold, 2004) and theses (Anderson, 1976; Panno, 1978). Additionally, Ryan (1981) and Seeger et al. (1989) reviewed the existing models for the ore-forming processes based on existing data. Two dominant hypotheses for the formation of the PKH deposit were proposed previously:

(i) The bedded hematite of the PKH deposit was chemically precipitated as a sedimentary iron formation in a shallow lake environment based on sedimentary features such as ripple marks and mud cracks (Anderson, 1976; Hauck, 1990; Dudley and Nold, 2004).

(ii) The bedded ore formed from hydrothermal fluids where the fluids infiltrated through and replaced the volcanoclastic precursor rocks while preserving preexisting sedimentary features (Kisvarsanyi and Proctor, 1967; Ryan, 1981; Panno and Hood, 1983).

Although the two hypotheses disagree on the ore-forming mechanisms, all studies agreed on a shallow emplacement level for the bedded ore, for example at the bottom of–or just beneath–a shallow caldera lake that periodically dried out, as evidenced by locally abundant mud cracks and rain drop or ash fall marks (Fig. 3D, E). However, it is noted that none of the previous studies discussed the origin of the brecciated ore in the agglomerate unit, although the volcanic agglomerate itself was inferred to be deposited in a caldera lake based on local bedded features (Panno, 1978; Seeger et al., 1989). The data presented here allow new constraints on the formation of the bedded and overlying brecciated ore of the PKH deposit.

Petrographic observations of the fine-grained, 5-18-meter-thick *bedded hematite* zone show that the ore is composed of specular hematite (Fig. 6) associated with sericite and mosaic-textured secondary quartz (Fig. 5). Such sericitization and silicification (hydrolytic) alteration assemblages are common in hematite-dominated upper portions of felsic-hosted IOA/IOCG systems and are caused by low-temperature (150-250°C) hydrothermal events (Oreskes and Einaudi, 1990; 1992; Hitzman et al., 1992; Bastrakov et al., 2007; Skirrow, 2010; Barton, 2014; Schlegel et al., 2018). The presence of euhedral quartz grains embaying into specular hematite (Fig. 6C) further supports the presence of a hydrothermal fluid (Rusk et al., 2008). It is noted that similar euhedral quartz grains are also reported from the magnetite-silicate zones of the magmatic-hydrothermal PKM deposit (Nold et al., 2013). Consequently, these petrographic observations favor a hydrothermal ore genetic model and are in agreement with the previously suggested replacement model by Kisvarsanyi and Proctor (1967), Ryan (1981), and Panno and

Hood (1983), rather than chemical precipitation of iron from shallow lake waters where much cooler temperatures would be expected.

The *brecciated samples* from the volcanic agglomerate unit contain single and aggregated crystals of primary hematite as well as secondary hematite with ilmenite exsolutions (Fig. 7). The presence of ilmenite exsolutions within the hematite aggregates (Fig. 7C, F) is interpreted that these hematite grains initially crystallized as Ti-rich magmatic magnetite (that was subsequently oxidized to hematite). Ilmenite exsolution forming a trellis-sandwich type texture along the {111} plane of the host magnetite as shown in Figure 7F commonly occurs as a result of oxy-exsolution of a high temperature (>400°C), Ti-rich magnetite (Ondrejka et al., 2015). In addition to the primary hematite aggregates, the PKH deposit also contains specular hematite, which is indicative of a hydrothermal origin brecciated ore (Hall et al., 1988; Cabral and Rosière, 2013). Based on these observations, we suggest that magmatic magnetite with high Ti content was erupted and reworked during a volcanic event, and then deposited with other erupted materials in a caldera lake, which is in agreement with the depositional caldera lake environment for the agglomerate unit suggested by Panno (1978). The volcanic agglomerate was subsequently infiltrated by a hydrothermal fluid that precipitated the specular hematite (Fig. 7) and oxidized magmatic magnetite to hematite, resulting in the hematite-ilmenite patterns shown in Figures 7C and 7F. Consequently, the petrographic observations discussed here are more consistent with a hydrothermal replacement origin with preserved pre-existing structures rather than a chemical precipitation model. It is noted that such a hydrothermal model for both the bedded and brecciated ore could represent the same fluid event, wherein the different textures would merely reflect the different textures of the infiltrated rocks.

5.2.2 Insight from oxide mineral chemistry

Minor and trace element substitution in iron oxide minerals is highly dependent on temperature and oxygen fugacity and has been shown to occur in greater amounts at higher temperature and reducing conditions (Dupuis and Beaudoin, 2011; Nadoll et al., 2014). Therefore, determining the minor and trace element composition of iron oxides provides insight into the ore-forming environment (e.g., Dupuis and Beaudoin, 2011; Dare et al., 2012; Nadoll et al., 2012; Dare et al., 2014; Nadoll et al., 2014). The elevated content of titanium in hematite is noteworthy and could be an indicator of a hydrothermal origin. Titanium is generally considered

to be immobile in hydrothermal systems due to the low solubility of rutile (Tropper and Manning, 2005; Dare et al., 2014). However, experimental studies by Rapp et al. (2010) and Tanis et al. (2016) have shown that Ti is mobile in halogen-rich hydrothermal fluids over wide range of pressures (0.5-2.79 GPa) and temperatures (250°C-1000°C). Specifically, Ti solubility is 2-4 times higher in chloride-brines than in H_2O, whereas the solubility is 20-100 times higher in fluoride-bearing brines (Rapp et al., 2010). Empirically, hydrothermal specularite at the Timbopeba itabirite-hosted hematite deposit in the Quadrilatero Ferrifero, Brazil, has been shown to contain Ti-bearing saline fluid inclusions with >30 wt.% NaCl equivalent and a formation temperature of 130°C-190°C (Rosière and Rios, 2006). Similarly, specularite at the Tilkerode selenide vein-type deposit in the Harz Mountains, Germany, contains Ti values from <420 ppm up to 8300 ppm and formed at <150°C (Cabral et al., 2011; Cabral and Rosière, 2013).

Hematite grains from the PKM contain Ti between 600 ppm to values as high as 45,000 ppm (average of 31,000 ppm) while martite (i.e. a hematite pseudomorph after magnetite) from the PKM contain <120 ppm (lower level of detection) to 4,800 ppm (average of 700 ppm) (Appendix A-1). Hematite grains from the PKH deposit have Ti concentrations between <120 ppm to 26,800 ppm (bedded ore; average of 3,800 ppm) and 17,000 ppm (agglomerate ore; average of 4,000 ppm, excluding secondary hematite grains with ilmenite exsolutions; Fig. 8B, Table 2). The highly variable Ti concentrations in hematite from the PKM and PKH deposits are notably higher than in PKM magnetite which contains between <120 ppm to 8,500 ppm Ti (average of 1,400 ppm; Fig. 8B, Table 2) whereas Ti contents in martite from the PKM are less compared to magnetite and hematite from the PKM and hematite from the PKH. These features (i.e., the higher Ti contents and variability in hematite compared to magnetite) are similar to observations made for hematite from the Mantoverde IOCG deposit in the Chilean iron belt and Rektorn IOA deposit in Norrbotten district of northern Sweden where the hematite is suggested to have crystallized from magmatic-hydrothermal fluids (Broughm et al., 2017; Childress et al., 2020). At Mantoverde, hematite was shown to have precipitated from hydrothermal fluids with salinities between 32 and 64 wt.% of NaCl equivalent and a temperature of 208°C-468°C based on fluid inclusion analyses (Rieger et al., 2012). By inference, abundant hydrothermal fluorite and rutile in the PKM deposit (Nold et al., 2013) and magmatic-hydrothermal fluorapatites in the nearby Pea Ridge and Boss deposits (Mercer et al., 2020) imply the magmatic-hydrothermal

fluids that facilitated Fe oxide mineralization in southeast Missouri contained some Cl and F. The presence of salt hoppers, as noted by Anderson (1976) and Panno (1978), provides additional evidence for highly saline fluid. Consequently, it is suggested that hematite in both the bedded unit and volcanic agglomerate of the PKH deposit precipitated from a highly saline hydrothermal fluid with a temperature of >130°C. However, it is noted that the presence of barite in some samples also suggests some input of surface water, possibly draw down of evaporitic water sourced from a periodically dried caldera lake. This is not surprising, since fluid mixing with possibly evaporitic waters sourced from a caldera lake has been suggested to have an important role in ore deposition (Barton and Johnson, 1996; Williams et al., 2005).

5.2.3 Insight from iron isotope chemistry

Iron isotope studies have been broadly carried out to constrain the physico-chemical processes that led to iron ore deposits such as IOA/IOCG-type (Sun et al., 2013; Weis, 2013; Bilenker et al., 2016; Childress et al., 2016; Troll et al., 2019), hydrothermal Fe ore deposits (Graham et al., 2004; Markl et al., 2006) and Banded Iron Formations (BIFs; Frost et al., 2007; Mendes et al., 2017; Hu et al., 2020). The iron isotope compositions of bedded hematite from the PKH deposit range from 0.05‰ to 0.30‰ with an average value of 0.13‰. Hematite from the brecciated samples is characterized by δ^{56}Fe values from -0.19‰ to 0.01‰. The δ^{56}Fe values of hematite overall display a narrow variability (Fig. 9, Table 3), which contradicts with what would have been expected if bedded hematite was of sedimentary origin, such as in BIFs, as such ores are commonly characterized by highly variable δ^{56}Fe signatures between -2.5‰ and +2.2‰ on a deposit scale reflecting significant Fe fractionation during sedimentation, including redox processes and Rayleigh type fractionation (Bullen et al., 2001; Johnson et al., 2003; Balci et al., 2006; Dauphas et al., 2007; Frost et al., 2007). Consequently, we argue that the δ^{56}Fe iron composition of hematite is more consistent with a hydrothermal origin than a sedimentary iron formation in a shallow lake environment, which is in agreement with the petrographic and mineralogical observations above. The similarities of iron isotopic compositions of the bedded and brecciated ore suggest that both ore horizons reflect formation in response to infiltration by the same or at least similar hydrothermal fluids. It is noted that the iron isotope compositions of the bedded and brecciated hematite fall within the global range of igneous rocks (0 – 0.85‰; Poitrasson and Freydier, 2005; Heimann et al., 2008; Craddock and Dauphas, 2011; Bilenker et

al., 2016), suggesting that the iron's provenance likely was magmatic. It is noted that hematite from the sample that contains the hematite/ilmenite exsolution pattern (DS-PK-F1; Fig. 7D to F) yielded a notably lower iron isotopic value of $\delta^{56}Fe$ = -0.19‰. This low value is interpreted to reflect extensive hydrothermal alteration, and/or complete or partial dissolution of iron and re-precipitation (*cf.* Weis, 2013), which is consistent with the petrographic observations discussed above. The remaining values cluster close to 0‰ and show less variation as opposed to sedimentary and/or supergene hydrothermal ores (Markl et al., 2006).

5.2.4 Insight from bulk rock chemistry

C1-chondrite normalized REE plots of clast-free hematite-mineralized samples from the bedded section of the PKH deposit, where Fe_2O_{3T} ranges between 34 wt.% and 80 wt.% (A-3), are characterized by concave-shaped REE pattern with pronounced LREE enrichment and a positive Eu anomaly (Fig. 12A, C). These features are in conjunction with the petrographic observations that imply the presence of an acidic hydrothermal fluid(s) that carried the LREE as chloride complexes and concentrated them (Oreskes and Einaudi, 1990; Haas et al., 1995). The positive Eu anomaly (Eu/Eu* = 1.2 – 4.8; Fig. 12A, C) implies that Eu was carried in a divalent state as chloride complex in an acidic hydrothermal fluid with temperatures between 200°C - 250°C (Sverjensky, 1984; Michard, 1989; Migdisov and Williams-Jones, 2014). In such a scenario, Eu was likely derived from hydrothermal alteration of plagioclase from the wall-rock rhyolites, which enriched the fluid in Eu (Arribas et al., 1995; Mao et al., 2016). Such acidic and highly saline hydrothermal fluids can carry up to 2000 ppm Fe at 400°C and 1 *m* of total chloride (Hemley et al., 1986), and cooling along with a decrease in salinity at shallower levels likely facilitated the precipitation of abundant hematite. Oxidized evaporite-sourced water also must have played a role in the formation of the hematite mineralization as implied by the positive Ba and Sr peaks observed in the PKH ore (Fig. 12B) that represent the presence of barite (Fig. 6F), which likely formed upon mixing of the hydrothermal fluid with a evaporitic fluid (Barton, 2014; Kreiner and Barton, 2017). The highly saline and acidic hydrothermal solutions that carried Fe and REE as chloride complexes likely also enriched the PKH ores with As, Sb, Sn, Mo, and W compared to that of the PKM ore (Fig. 13). The capability of Cl- and F-bearing acidic fluid mobilizing incompatible elements from the source have been discussed elsewhere (McPhie et al., 2011). For example, at the Olympic Dam deposit, hematite precipitated from hydrothermal fluids

is characterized by enrichment of W, Mo, Sn, As, and Sb which reflects a hydrothermal fluid that was also enriched in these elements (Ciobanu et al., 2013; Verdugo-Ihl et al., 2017).

5.2.5 Summary of observations and implications for the formation of the PKH deposit

In summary, the data presented in this study suggest that hematite from both the bedded and brecciated hematite ore of the PKH deposit are of hydrothermal rather than sedimentary origin. The petrographic observations of the bedded hematite section suggest that hematite crystallized from hydrothermal fluids that developed sericitic and silicic alteration assemblages, most likely at temperatures between 150°C-250°C. This hypothesis is supported by elevated Ti concentrations in PKH hematite which suggest that hematite is precipitated replacing the volcanoclastic rocks from a highly saline hydrothermal fluid with a temperature of >130°C. Additionally, the iron isotope compositions of hematite from PKH imply a magmatic source for the Fe and subsequent hydrothermal transport and deposition. The bulk rock chemistry of hematite-mineralized samples from the PKH also suggests that hematite formed through hydrothermal replacement from highly saline and acidic hydrothermal fluid at temperatures between 200°C and 250°C. However, it is noted that the presence of barite in some samples implies that the hematite mineralization may have been aided by fluid mixing with evaporitic waters sourced from a caldera lake, which is not surprising due to the shallow emplacement level of the ore.

5.3 Genetic relationship between the PKM and PKH deposit

Although the PKM and PKH are separated stratigraphically by only 240 m, a possible relationship between two deposits with regards to ore-forming mechanism has not been broadly discussed. Panno and Hood (1983), who suggested a hydrothermal origin for the PKH deposit, were the first to speculate that a genetic link between the two deposits may exist, i.e., that the PKH is an updip projection of the PKM deposit. However, Anderson (1976), who proposed a sedimentary origin for the PKH deposit, claimed that the PKM and PKH deposits have different origins.

The data presented here suggest that bedded and brecciated ores of the PKH deposit formed from a highly saline and acidic hydrothermal fluid with temperature of probably 200°C - 250°C. In contrast, the PKM deposit has previously been proposed to be of magmatic and

magmatic-hydrothermal origin (Panno and Hood, 1983; Nold et al., 2013; Childress et al., 2016). The PKM magnetite data presented here are characterized by low Ti and V contents in plots of Ti vs. V and Fe vs. V/Ti , thus implying a hydrothermal PKM magnetite origin (Fig 14 A, B). The hydrothermal magnetite, as indicated by these binary plots, also does not show any re-equilibration trend of hydrothermally overprinted magmatic magnetite (Fig. 14B). Therefore, based on the magnetite chemistry, we interpret that the magnetite in our samples precipitated from highly saline and acidic magmatic-hydrothermal fluids with temperatures between 200°C and 500°C, which is in agreement with previous studies by Panno and Hood (1983), Nold et al. (2013), and Childress et al. (2016) although the magmatic-hydrothermal magnetite may be significantly more abundant than magmatic magnetite in the PKM, as, for example, observed in the nearby Pea Ridge deposit (Johnson et al., 2016). The magmatic-hydrothermal fluids likely migrated upward and precipitated abundant hematite at cooler temperatures of ~200-250°C and higher oxygen fugacity upon infiltration of surface-near sedimentary structures (i.e., bedded and brecciated units). It is noted that the guidebook by Ryan (1981) described a magnetite-cemented breccia at the northwestern flank of the Pilot Knob mountain where hematite partially replaced the magnetite which the author suggested may represent a fluid pathway that connected the PKM with the near-surface PKH deposit.

Precipitation of hematite from orthomagmatic ore fluids is supported by the fact that hematite from both PKM and PKH share the same origin, based on their similar chemistry, wherein hematite in both deposits have similarly elevated concentrations of Ti, despite the variability (Fig. 8A, B). Additionally, the $\delta^{56}Fe$ values of the upper hematite of the PKH ($\delta^{56}Fe$ = 0.05~0.30‰, average of 0.13‰; Fig. 9, Table 3) are overall slightly depleted compared to that of magnetite ore of the PKM ($\delta^{56}Fe$ = 0.06~0.27‰, average of 0.17‰; Childress et al., 2016), with both isotopic signatures falling within the range for a magmatic source. Similar features are observed between the magnetite and hematite Fe isotopic signatures of the Mantoverde deposit, where the iron isotopic compositions of hematite (0.34 to 0.46‰) are slightly lighter than that of magnetite (0.46‰ to 0.58‰) (Childress, 2019). Magnetite mineralization at Mantoverde occurs at a deeper level, with formation temperatures between 278 - 530°C compared to shallower hematite mineralization with formation temperatures of 208 - 468°C (Rieger et al., 2012; Childress, 2019). Textural evidence of hematite, i.e., occurring in veinlets, and its lower formation temperature at Mantoverde indicates a late stage hydrothermal fluid formation of the

hematite ore (Childress, 2019). Based on the Fe isotopic signatures at Mantoverde, it has been proposed that magnetite and hematite precipitated from Fe-rich magmatic-hydrothermal fluids exhibit a similar isotopic signature (Childress, 2019). Similar to the observations made for Mantoverde, the data for PKM magnetite (0.06‰ – 0.27‰) and overlying PKH hematite (0.05‰ - 0.30‰) have comparable isotopic signatures (Fig. 9, Table 3). Consequently, it is plausible that the bedded and brecciated PKH hematite ore precipitated from the same hydrothermal fluid that precipitated the PKM magnetite at a deeper level.

The similar patterns in C1 chondrite-normalized rare earth element and bulk silicate Earth normalized multi-element diagrams of the PKM (Fe_2O_{3T} = 16-89 wt.%) and PKH (Fe_2O_{3T} = 34-80 wt.%) ores (Fig. 12) also imply that the iron ore deposits have a shared origin, i.e., that both magnetite and hematite originated from acidic magmatic-hydrothermal fluids that circulated through volcanic rocks at different levels. Accordingly, magnetite likely crystallized from a more reducing and hotter fluid at deeper levels whereas hematite is crystallized from more oxidizing and cooler fluid at shallower levels. In summary, based on the isotopic, mineral and bulk rock chemical signatures presented here, we suggest that the PKM and PKH deposits are two endmembers of a high- to low-temperature magmatic-hydrothermal continuum, similar to other IOA/IOCG systems such as Mantoverde and Prominent Hill (Benavides et al., 2008; Skirrow, 2010).

5.4 Implication for the regional scale formation of iron ore deposits in SE Missouri

The tectono-magmatic environment that led to the formation of the IOA/IOCG type deposits in the St. Francois Mountains region remains controversial. A number of studies suggested that the granite-rhyolite terrane developed in a continental rift setting due to a mantle plume localized beneath a Proterozoic supercontinent (Kisvarsanyi, 1981; Hitzman, 2000; Lowell, 2000; Groves et al., 2010). However, other studies, such as by Menuge et al. (2002) and Walker et al. (2002), advocated a continental back-arc setting associated with convergent tectonism for the development of the EGR terrane based on geochemistry of granitoids. Recent studies by Day et al. (2016) and Watts and Mercer (2020) reevaluated the tectonic setting and claimed that the St. Francois Mountains terrane formed during an extensional regime developed on a continental arc setting of the supercontinent Laurentia.

715 The bulk rock data presented in this study identify the host volcanic rocks of the PKM
716 deposit as rhyolites and rhyodacites (Fig. 11A). The rocks are characterized as A2 type granites
717 based on immobile trace element chemistry and appear to have been emplaced in an extensional
718 environment related to convergent tectonism (Fig. 11D). It is noted that the absence of a Eu
719 anomaly (Fig. 12A) and a negative trough of Nb and Ta in the multi-element spidergram (Fig.
720 12B) imply a hydrous environment, as water suppresses plagioclase fractionation in magmas
721 (Loucks, 2014) and Nb and Ta are highly water-insoluble (Adam et al., 2014). Thus, our data
722 suggest a subduction-modified hydrous source for the rhyolites and rhyodacites, likely derived
723 from a subcontinental lithospheric mantle (SCLM) that was metasomatized by fluids released
724 from the subducted slab in one or more pulses–similar to observations made for other variably
725 hydrated ore deposits in post-collisional settings (Holwell et al., 2019; Fiorentini et al., 2019;
726 Locmelis et al., 2020). This interpretation is in agreement with the model by Day et al. (2016)
727 that suggests that multiple pulses of magmatism derived from both mantle and crust were
728 involved in the formation of the St. Francois Mountain Terrane based on Nd isotopic data.
729 Similarly, Watts and Mercer (2020) suggested that parental magmas of the Pea Ridge and
730 Bourbon deposits were sourced from a subduction-metasomatized lithospheric mantle based on
731 melt inclusions with high K and Cl concentrations in zircons from these deposits. These authors
732 also point out that multiple injections of mafic magmas provided Cl into the evolving silicic
733 magma and/or coexisting silicic melt from which Cl-rich hydrothermal fluids exsolved. This Cl-
734 rich hydrous magma and subsequent exsolution of hypersaline fluids which carried Fe
735 complexed with Cl are likely responsible for several regional ore-forming events, based on the
736 spatial and temporal proximity of Missouri's iron ore deposits (Fig. 1; Day et al., 2016; Watts
737 and Mercer, 2020). For example, the timing of iron and REE mineralization at the Pea Ridge
738 IOA deposit spans episodically from the main mineralization stage at 1469 Ma (Neymark et al.,
739 2016a) to a late crosscutting leucogranitic dike which limits the lower age of magmatism dated at
740 1441±9 Ma (Aleinikoff et al., 2016; Neymark et al., 2016a). Neymark et al. (2016b) reported
741 preliminary age results of ~1.45 Ga on apatite grains from the Kratz Spring, Bourbon, and Iron
742 Mountain deposits (Fig. 1). Based on the zircon U-Pb method, Watts and Mercer (2020)
743 demonstrated that the initial magmatism at Bourbon occurred ~1500 Ma and hydrothermal event
744 occurred ~1442 Ma. The new age constraint for the PKM deposit provided in this study is ~1438
745 Ma, which is approximately 30 Ma younger than the ages of nearby volcanic ash flow tuffs and

746 rhyolites (Bickford et al., 2015) and falls within the lower age limit of magmatism at Pea Ridge
747 and Bourbon (Aleinikoff et al., 2016; Neymark et al., 2016a; Watts and Mercer, 2020). These
748 age constraints imply that the hydrous magmatism and the associated exsolution of a
749 metalliferous hydrothermal fluid continued episodically for at least 60 Myrs and formed the local
750 cluster of IOA and IOCG type deposits in southeast Missouri.

751 This interpretation is in agreement with the model by Ayuso et al. (2016) that utilized Nd
752 and Pb isotopes to show that the magma that generated the rhyolites and rhyodacites and, by
753 extension, the spatially associated Fe oxide deposits in southeast Missouri, was sourced from 1.5
754 Ga or younger juvenile lower crust and SCLM, which is indicated by the Nd line shown in
755 Figure 1 that separates the younger basement (Nd model age < 1.5 Ga) from the older basement
756 with Nd model age > 1.5 Ga (Bickford et al., 2015). Additionally, Day et al. (2016) reevaluated
757 the tectono-magmatic setting of the St. Francois Mountains region during the 1.50-1.44 Ga
758 period and suggested that the terrane developed on a growing continental margin that
759 transitioned into an extensional regime, which triggered extensive magmatism. Similar examples
760 occur around the world, such as in the Chilean Iron Ore Belt, although significantly younger,
761 where iron oxide deposits formed through magmatic and magmatic-hydrothermal processes (e.g.,
762 Bilenker et al., 2016; Simon et al., 2018). Older examples include the Olympic Dam IOCG-type
763 deposits in South Australia and Kiruna-type deposits in Sweden, of which the tectonic settings
764 are also concluded to be subduction-related extension where the SCLM was the source for
765 economically significant iron oxide mineralization (e.g., Reid, 2019). In this extensional tectonic
766 environment developed on Laurentia, Kisvarsanyi and Proctor (1967) and Day et al. (2016)
767 suggested that mafic to intermediate magma sourced from the subduction-modified SCLM and
768 subsequent fluid exsolution are responsible for the IOA and IOCG-type deposits distributed in
769 southeast Missouri. In such a context, the Pilot Knob system may be a shallow and small-scale
770 snapshot of processes similar to the ones that form the IOA-IOCG continuum, i.e., a deeper
771 magmatic event that exsolved a hydrothermal fluid that forms an overlying ore body.

772 **6. Conclusions**

773 The early Mesoproterozoic St. Francois Mountains igneous terrane in southeast Missouri
774 hosts several IOA and IOCG-type deposits. This study focused on the Pilot Knob Hematite

deposit and the Pilot Knob Magnetite deposit, which is located 240 m stratigraphically beneath the hematite deposit. Our findings show that:

- The mineralization age of the PKM deposit is constrained to be 1437.7±5.8 Ma based on U-Pb of apatite that co-crystallized with magnetite.
- The PKH deposit is of hydrothermal origin based on ore petrography, iron oxide, iron isotope, and bulk rock chemistry.
- The PKM deposit and PKH deposits are genetically related. The ore fluid(s) exsolved from the hydrous magma that facilitated the formation of the PKM deposit migrated upwards and precipitated hematite ore near the surface.
- The Mesoproterozoic St. Francois Mountains igneous terrane developed on a growing continental arc and the iron oxide deposits in the region formed during the transition from convergent to extensional regime in association with an episodic magmatism that lasted for ~60 Myrs.
- The Pilot Knob Magnetite and Hematite deposits possibly represent a shallow and small-scale snapshot of processes similar to the ones that form the IOA-IOCG continuum, i.e., a deeper magmatic event that exsolved a hydrothermal fluid that forms an overlying ore body.

7. Acknowledgements

This paper is part of B. N. T.'s Ph.D. thesis at Missouri S&T. B. N. T. acknowledges funding through a Radcliffe Graduate Scholarship in the Geology & Geophysics program at Missouri S&T. M. L. acknowledges funding through the NSF CAREER award 1944552 "Investigating the source, transport and deposition of economically important metals in the lower continental crust". Authors also acknowledge Corey Kudrna from the Mingo National Wildlife Refuge and Russell Myers from the Mars Geosciences US Inc. for their open conversation, guidance, and help in the field. Paul Carpenter is thanked for help with the electron microprobe analysis. David Wronkiewicz, David Borrok and Kwame Awuah-Offei are thanked for insightful comments during the preparation of this manuscript. This manuscript has greatly benefited from critical reviews by Adam Simon and two anonymous reviewers. We thank Huayong Chen and Zhaochong Zhang for the editorial handling. This is contribution #9 of the Missouri S&T MCTF research group and a publication of the O'Keefe Institute for Sustainable Supply of Strategic Minerals at Missouri University of Science and Technology.

Figures

Fig. 1. A. The Granite-Rhyolite terrane (1500-1350 Ma) in the midcontinent region of the United States (modified after Van Schmus et al. (1996). The white rectangle depicts the location of the St. Francois Mountains terrane. B. Simplified geological map showing basement igneous rocks in the St. Francois Mountains terrane (modified after Day et al. (2016)). C. Geological map of Precambrian outcrops in the St. Francois Mountains terrane (modified after Pratt et al. (1979)).

Fig. 2. A. Surface geological map of the Pilot Knob area in Southeast Missouri showing the shaft to the Pilot Knob Magnetite subsurface deposit and the location of the Pilot Knob Hematite deposit on top of the Pilot Knob Mountain (modified after Ryan (1981)). B. Simplified stratigraphy of the Pilot Knob Magnetite and Pilot Knob Hematite deposits (modified after Ryan (1981) and Panno and Hood (1983)). C. Detailed stratigraphic column of the ore beds of the Pilot Knob Hematite deposit (modified after Ryan (1981)).

Fig. 3. Representative field and drill core images of the PKH and PKM deposits. A. Outcrop and open pit workings of the PKH deposit; B. Boulder of bedded hematite from the Lower Ore Bed in the PKH deposit; C. Bedded hematite from the Upper Ore Bed in the PKH deposit; D. Outcrop in the PKH deposit showing ripple marks; E. Hand sample from the PKH deposit showing raindrop marks; F. Boulder showing the Volcanic Agglomerate unit of the PKH deposit. G. Drill core sample of the PKM deposit showing disseminated ore at a depth of 625.8 m (PKM-1160-2053); H. Drill core sample of the PKM deposit showing massive ore at a depth of 636.4 m (PKM-1160-2088); I. Drill core sample of the PKM deposit showing impregnated ore at a depth of 666.9 m (PKM-1160-2188); J. Drill core sample of the PKM deposit showing brecciated ore at a depth of 669.3 m (PKM-1160-2196).

Fig. 4. Representative reflected light microscopy and back scattered electron (BSE) images of samples from the PKM deposit. A. Massive magnetite with rutile (reflected light, PKM-1160-2038); B. Massive magnetite with rutile and minor hematite replacement along grain boundaries (reflected light, PKM-1160-2188); C. Disseminated magnetite with trace pyrite and molybdenite (reflected light, PKM-1160-2053); D. Euhedral to subhedral disseminated magnetite partially altered to martite with anhedral hematite (reflected light, PKM-1098-580); E. Massive magnetite with ilmenite and barite inclusions (BSE, PKM-1160-2038); F. Massive magnetite with apatite (BSE, PKM-1160-2105). Abbreviations: Mag – magnetite, Hem – hematite, Py – pyrite, Mol – molybdenite, Ilm – ilmenite, Apt – apatite, Bar – barite, Rut – rutile.

Fig. 5. Representative transmitted light images with crossed polarizers of bedded hematite samples from the PKH deposit. A. Bedded hematite from the Lower Ore Bed showing euhedral to subhedral quartz with sericite (PcF-071); B. Mosaic-textured quartz with sericite (PcF-061); C. Subhedral to anhedral quartz with sericite (PcF-071); D. Bedded hematite from the Lower Ore Bed (PcF-061) in which primary quartz grain is overgrown with secondary mosaic quartz; E. Bedded hematite from the Lower Ore Bed showing sericite surrounding hematite (PcF-073); F. Secondary quartz with sericite (PcF-073). Abbreviations: Qz – quartz, Ser – sericite, Hem – hematite.

Fig. 6. Representative reflected light and back scattered electron (BSE) images of bedded ore samples from the PKH deposit A. Image of a polished mount with bedded hematite (reflected light,

DS-PK-F2); B. Single and aggregated crystals of hematite in the sample shown in 6A (reflected light); C. Single specular and aggregated crystals of hematite with euhedral, hexagonal quartz in the sample shown in 6A (BSE); D. Image of a polished mount showing the bedded hematite texture (reflected light, PK-1156); E. Single specular and aggregated crystals of hematite in the sample shown in 6D (reflected light, PK-1156); F. Hematite with barite in the sample shown in 6D (BSE, PK-1156). Abbreviations: Bar – barite, Hem – hematite, Qz – quartz.

Fig. 7. Representative reflected-light and back scattered electron (BSE) images of brecciated ore samples from the PKH. A. Image of a polished mount showing the brecciated hematite texture (reflected light, DS-PK-F1); B. Single specular and aggregated crystals of specular hematite in the sample shown in 7A.; C. Aggregated hematite crystal with ilmenite exsolutions in the same sample shown in 7A; D. Image of an entire polished mount showing the brecciated hematite texture (reflected light, UPK-F1); E. Hematite aggregates with a pyrite and ilmenite inclusions from the sample shown in 7D; F. BSE image of hematite with trellis-sandwich type texture reflected by ilmenite exsolution and intergrown zircon from the sample shown in 7D. Abbreviations: Hem – hematite, Ilm – ilmenite, Py – pyrite, Zr – zircon.

Fig. 8. Multi-element box and whisker plots for electron microprobe minor and trace element data for magnetite and hematite. A. Magnetite and hematite from the PKM deposit. B. Primary (yellow) and secondary (purple) hematite with ilmenite exsolutions from the volcanic agglomerate and bedded hematite units (green) of the PKH deposit. Boxes outline the 25^{th} to 75^{th} percentile and whiskers extend to the minimum and maximum values. The short line within the box represents the median value, whereas circle filled by white on the whisker plot represents the average value. Numbers indicate the percentage of analyses that are above detection limits for each element.

Fig. 9. The stable iron isotope chemistry ($\delta^{56}Fe$) of magnetite and hematite/specularite from the Pilot Knob deposits. Samples from the Mantoverde IOCG deposit are shown for comparison. The reported values of this study are an average of two different measurements. Error bars indicate the conservative errors of the variations of the standard. Data sources: 1 = Childress (2019), 2 = Childress et al. (2016).

Fig. 10. Tera-Wasserburg plot of apatite U-Pb geochronology result on sample PKM-1160-2105. In this plot, 6 data are rejected and anchor composition of 207/206 ratio is 0.95.

Fig. 11. A. Bulk rock Nb/Y vs. Zr/Ti plot (after Winchester and Floyd, 1977); B. Bulk rock Y vs. Nb (after Pearce et al., 1984); C. Bulk rock $Ga*10^4/Al$ vs. Nb plot (after Whalen et al., 1987); D. Bulk rock Y/Nb vs. Sc/Nb plot (after Eby, 1992). Abbreviations: VAG: Volcanic arc granites, syn+COLG: Collision granites, WPG: Within plate granites, and ORG: Ocean ridge granites.

Fig. 12. A. C1 chondrite-normalized bulk rock REE spidergram; B. Bulk silicate Earth normalized multi-element bulk rock spidergram; C. Bulk rock Eu_n/Eu^* vs. Ce_n/Ce^* (where $Eu^*=Eu_n/SQRT(Sm_n x Gd_n)$ and $Ce^*=Ce_n/SQRT(La_n x Pr_n)$; D. Bulk rock $(La/Yb)_n$ vs. $(Dy/Yb)_n$ (where n denotes normalization to the C-1 chondrite). All normalizing values are from McDonough and Sun (1995).

Fig. 13. Bulk rock concentrations of As, Mo, Sb and W vs. Fe_2O_3 content.

884 **Fig. 14.** (A). Ti vs. V concentrations in magnetite from the PKM deposit (after Knipping et al.,
885 2015). (B). Fe vs. V/Ti concentrations in magnetite from the PKM deposit (after Wen et al., 2017).

886 **Tables**

887 Table 1. List of samples and sampling modes/locations.

888 Table 2. Summary of electron microprobe analysis of magnetite and hematite from the PKM and
889 PKH deposits.

890 Table 3. Summary of Fe stable isotope analysis of magnetite and hematite from the PKM and
891 PKH deposits.

892 **Appendix**

893 A-1. Magnetite and hematite electron microprobe data.

894 A-2. Apatite single-grain U-Pb geochronology data.

895 A-3. Bulk rock data.

896 **References**

897 Adam, J., Locmelis, M., Afonso, J.C., Rushmer, T., Fiorentini, M.L., 2014. The capacity of
898 hydrous fluids to transport and fractionate incompatible elements and metals within the
899 Earth's mantle. Geochem. Geophys. Geosystems 15, 2241-2253.
900 Aleinikoff, J.N., Selby, D., Slack, J.F., Day, W.C., Pillers, R.M., Cosca, M.A., Seeger, C.M.,
901 Fanning, C.M., Samson, I.M., 2016. U-Pb, Re-Os, and Ar/Ar geochronology of rare earth
902 element (REE)-rich breccia pipes and associated host rocks from the Mesoproterozoic
903 Pea Ridge Fe-REE-Au deposit, St. Francois Mountains, Missouri. Econ. Geol. 111, 1883-
904 1914.
905 Anderson, L.C., 1976. The Pilot Knob hematite deposit, Pilot Knob, southeast Missouri. Master's
906 thesis, University of Wisconsin-Madison, 80 p.
907 Arribas, A., Cunningham, C.G., Rytuba, J.J., Rye, R.O., Kelly, W.C., Podwysocki, M.H.,
908 McKee, E.H., Tosdal, R.M., 1995. Geology, geochronology, fluid inclusions, and isotope
909 geochemistry of the Rodalquilar gold alunite deposit, Spain. Econ. Geol. 90, 795-822.
910 Arundale, J., Martin, J.A., 1970. The mineral industry of Missouri. In: U.S. Bureau of Mines
911 1968 Minerals Yearbook. 3, 429-443.
912 Ayuso, R.A., Slack, J.F., Day, W.C., McCafferty, A.E., 2016. Geochemistry, Nd-Pb isotopes,
913 and Pb-Pb ages of the Mesoproterozoic Pea Ridge iron oxide-apatite–rare earth element
914 deposit, Southeast Missouri. Econ. Geol. 111, 1935-1962.
915 Balci, N., Bullen, T.D., Witte-Lien, K., Shanks, W.C., Motelica, M., Mandernack, K.W., 2006.
916 Iron isotope fractionation during microbially stimulated Fe(II) oxidation and Fe(III)
917 precipitation. Geochem. Cosmochim. Acta 70, 622-639.
918 Barton, M.D., 2014. Iron oxide (-Cu-Au-REE-P-Ag-U-Co) systems. Treatise on Geochemistry,
919 second ed. Elsevier Inc., 13, pp. 515-541.
920 Barton, M.D., Johnson, D.A., 1996. Evaporitic-source model for igneous-related Fe oxide–
921 (REE-Cu-Au-U) mineralization. Geology 24, 259-262.

Bastrakov, E.N., Skirrow, R.G., Davidson, G.J., 2007. Fluid evolution and origins of iron oxide Cu-Au prospects in the Olympic Dam district, Gawler craton, South Australia. Econ. Geol. 102, 1415-1440.

Beard, B.L., Johnson, C.M., Skulan, J.L., Nealson, K.H., Cox, L., Sun, H., 2003. Application of Fe isotopes to tracing the geochemical and biological cycling of Fe. Chem. Geol. 195, 87-117.

Benavides, J., Kyser, T.K., Clark, A.H., Stanley, C., Oates, C., 2008. Exploration guidelines for copper-rich iron oxide–copper–gold deposits in the Mantoverde area, northern Chile: The integration of host-rock molar element ratios and oxygen isotope compositions. Geochem-Explor. Env. A. 8, 343-367.

Bickford, M.E., Mose, D.G., 1975. Geochronology of Precambrian rocks in the St. Francois Mountains, southeastern Missouri. Geology 3, 537-540.

Bickford, M.E., Sides, J.R., Cullers, R.L., 1981. Chemical evolution of magmas in the Proterozoic terrane of the St. Francois Mountains, southeastern Missouri. 1. Field, petrographic, and major element data. J. Geophys. Res. 86, 10365-10386.

Bickford, M.E., Van Schmus, W.R., Karlstrom, K.E., Mueller, P.A., Kamenov, G.D., 2015. Mesoproterozoic-trans-Laurentian magmatism: A synthesis of continent-wide age distributions, new SIMS U–Pb ages, zircon saturation temperatures, and Hf and Nd isotopic compositions. Precambrian Res. 265, 286-312.

Bilenker, L.D., Simon, A.C., Reich, M., Lundstrom, C.C., Gajos, N., Bindeman, I., Barra, F., Munizaga, R., 2016. Fe–O stable isotope pairs elucidate a high-temperature origin of Chilean iron oxide-apatite deposits. Geochem. Cosmochim. Acta 177, 94-104.

Brandom, R.T., 1989. Ore microscopy and electron probe microchemical analysis of the Boss-Bixby deposit, southeastern Missouri. Master's thesis, University of Missouri-Rolla, 128 p.

Broughm, S.G., Hanchar, J.M., Tornos, F., Westhues, A., Attersley, S., 2017. Mineral chemistry of magnetite from magnetite-apatite mineralization and their host rocks: Examples from Kiruna, Sweden, and El Laco, Chile. Mineral. Deposita 52, 1223-1244.

Bullen, T.D., White, A.F., Childs, C.W., Vivit, D.V., Schulz, M.S., 2001. Demonstration of significant abiotic iron isotope fractionation in nature. Geology 29, 699-702.

Cabral, A.R., Lehmann, B., Tupinambá, M., Wiedenbeck, M., Brauns, M., 2011. Geology, mineral chemistry and tourmaline B isotopes of the Córrego Bom Sucesso area, southern Serra do Espinhaço, Minas Gerais, Brazil: Implications for Au–Pd–Pt exploration in quartzitic terrain. J. Geochem. Explor. 110, 260-277.

Cabral, A.R., Rosière, C.A., 2013. The chemical composition of specular hematite from Tilkerode, Harz, Germany: Implications for the genesis of hydrothermal hematite and comparison with the Quadrilátero Ferrífero of Minas Gerais, Brazil. Mineral. Deposita 48, 907-924.

Chen, M., Bagas, L., Liao, X., Zhang, Z., Li, Q., 2019. Hydrothermal apatite SIMS Th-Pb dating: Constraints on the timing of low-temperature hydrothermal Au deposits in Nibao, SW China. Lithos 324-325, 418-428.

Chew, D.M., Sylvester, P.J., Tubrett, M.N., 2011. U–Pb and Th–Pb dating of apatite by LA-ICPMS. Chem. Geol. 280, 200-216.

Childress, T.M., 2019. Fingerprinting source fluids of iron oxide-copper-gold and iron oxide-apatite deposits using traditional and non-traditional stable isotope geochemistry. Ph.D. dissertation, University of Michigan, Michigan, 196 p.

Childress, T.M., Simon, A.C., Day, W.C., Lundstrom, C.C., Bindeman, I.N., 2016. Iron and oxygen isotope signatures of the Pea Ridge and Pilot Knob magnetite-apatite deposits, southeast Missouri, USA. Econ. Geol. 111, 2033-2044.

Childress, T.M., Simon, A.C., Reich, M., Barra, F., Arce, M., Lundstrom, C.C., Bindeman, I.N., 2020. Formation of the Mantoverde iron oxide-copper-gold (IOCG) deposit, Chile: Insights from Fe and O stable isotopes and comparisons with iron oxide-apatite (IOA) deposits. Mineral. Deposita.

Ciobanu, C.L., Wade, B.P., Cook, N.J., Schmidt Mumm, A., Giles, D., 2013. Uranium-bearing hematite from the Olympic Dam Cu–U–Au deposit, South Australia: A geochemical tracer and reconnaissance Pb–Pb geochronometer. Precambrian Res. 238, 129-147.

Craddock, P.R., Dauphas, N., 2011. Iron isotopic compositions of geological reference materials and chondrites. Geostand. Geoanal. Res. 35, 101-123.

Crane, G.W., 1912. The iron ores of Missouri. Missouri Bureau of Geology and Mines. v. 10, 2nd Series, 434 p.

Cullers, R., Koch, R., Bickford, M., 1981. Chemical evolution of magmas in the igneous terrane of the St. Francois Mountains, Missouri, II. Trace element evidence. J. Geophys. Res. 86, 10365-10387.

Dare, S.A.S., Barnes, S.-J., Beaudoin, G., 2012. Variation in trace element content of magnetite crystallized from a fractionating sulfide liquid, Sudbury, Canada: Implications for provenance discrimination. Geochem. Cosmochim. Acta 88, 27-50.

Dare, S.A.S., Barnes, S.-J., Beaudoin, G., Méric, J., Boutroy, E., Potvin-Doucet, C., 2014. Trace elements in magnetite as petrogenetic indicators. Mineral. Deposita 49, 785-796.

Dauphas, N., Cates, N.L., Mojzsis, S.J., Busigny, V., 2007. Identification of chemical sedimentary protoliths using iron isotopes in the >3750 Ma Nuvvuagittuq supracrustal belt, Canada. Earth Planet. Sci. Lett. 254, 358-376.

Day, W., Seeger, C.M., Rye, R.O., 2001. Review of the iron oxide deposits of Missouri-magmatic end members of the iron oxide-Cu-Au-U-REE deposit family. Abstr. Programs Geol. Soc. Am. 33 (6), 4.

Day, W.C., Granitto, M., Ayuso, R., Slack, J., 2017. Geochemical database for iron oxide-copper-cobalt-gold-rare earth element deposits of southeast Missouri (August 2017): U.S. Geological Survey data release, http://dx.doi.org/10.5066/F7P26W67.

Day, W.C., Slack, J.F., Ayuso, R.A., Seeger, C.M., 2016. Regional geologic and petrologic framework for iron oxide ± apatite ± rare earth element and iron oxide copper-gold deposits of the Mesoproterozoic St. Francois Mountains terrane, southeast Missouri, USA. Econ. Geol. 111, 1825-1858.

Dudley, M.A., 1998. Geology and mineralogy of the Iron Mountain mine, St. Francois CO, Missouri. Master's thesis, University of Missouri-Rolla, 184 p.

Dudley, M.A., Nold, J.L., 2001. Mineralogy and ore textures of the Shepherd Mt. iron deposit, Iron Co., Missouri. Trans. Mo. Acad. Sci. 35, 58.

Dudley, M.A., Nold, J.L., 2003a. The Cedar Hill deposit, Iron county, MO: A Proterozoic oolitic sedimentary banded iron formation. Abstr. Programs Geol. Soc. Am. 35 (2), 11.

Dudley, M.A., Nold, J.L., 2003b. Occurrence and origin of the Hogan iron deposit, St. Francois Mountains, southeast Missouri. Trans. Mo. Acad. Sci. 37, 85.

Dudley, M.A., Nold, J.L., 2004. Sedimentary iron deposits within the St. Francois Mountains magmatic-hydrothermal iron district, southeast Missouri. Abstr. Programs Geol. Soc. Am. 36 (5), 446.

Dunkl, I., Mikes, T., Simon, K., von Eynatten, H., 2008. Brief introduction to the Windows program Pepita: data visualization, and reduction, outlier rejection, calculation of trace element ratios and concentrations from LA-ICP-MS data, in: Sylvester, P.J. (Ed.), Laser ablation ICP-MS in the Earth Sciences. Mineralogical Association of Canada, Short Course, 40, pp. 334-340.

Dupuis, C., Beaudoin, G., 2011. Discriminant diagrams for iron oxide trace element fingerprinting of mineral deposit types. Mineral. Deposita 46, 319-335.

Eby, G.N., 1992. Chemical subdivision of the A-type granitoids: Petrogenetic and tectonic implications. Geology 20, 641-644.

Fiorentini, M.L., LaFlamme, C., Denyszyn, S., Mole, D., Maas, R., Locmelis, M., Caruso, S. and Bui, T.H., 2018. Post-collisional alkaline magmatism as gateway for metal and sulfur enrichment of the continental lower crust. Geochim. Cosmochim. Acta, 223, 175-197.

Frost, C.D., von Blanckenburg, F., Schoenberg, R., Frost, B., Swapp, S., 2007. Preservation of Fe isotope heterogeneities during diagenesis and metamorphism of banded iron formation. Contrib. Mineral. Petrol. 153, 211.

Graham, S., Pearson, N., Jackson, S., Griffin, W., O'Reilly, S.Y., 2004. Tracing Cu and Fe from source to porphyry: in situ determination of Cu and Fe isotope ratios in sulfides from the Grasberg Cu–Au deposit. Chem. Geol. 207, 147-169.

Groves, D.I., Bierlein, F.P., Meinert, L.D., Hitzman, M.W., 2010. Iron oxide copper-gold (IOCG) deposits through earth history: Implications for origin, lithospheric setting, and distinction from other epigenetic iron oxide deposits. Econ. Geol. 105, 641-654.

Haas, J.R., Shock, E.L., Sassani, D.C., 1995. Rare earth elements in hydrothermal systems: Estimates of standard partial molal thermodynamic properties of aqueous complexes of the rare earth elements at high pressures and temperatures. Geochem. Cosmochim. Acta 59, 4329-4350.

Hall, D.L., Cohen, L.H., Schiffman, P., 1988. Hydrothermal alteration associated with the Iron Hat iron skarn deposit, eastern Mojave Desert, San Bernardino County, California. Econ. Geol. 83, 568-587.

Hauck, S.A., 1990. Petrogenesis and tectonic setting of middle Proterozoic iron oxide–rich ore deposits: An ore deposit model for Olympic Dam-type mineralization, in: Pratt, W.P., Sims, P.K. (Eds.), The Midcontinent of the United States-Permissive Terrane for an Olympic Dam-Type Deposits. U.S. Geological Survey., Denver, CO, Midcontinent Strategic and Critical Minerals Project 1988, Workshop Report, pp. 4-39.

Heidarian, H., Lentz, D.R., Alirezaei, S., McFarlane, C.R.M., Peighambari, S., 2018. Multiple stage ore formation in the Chadormalu iron deposit, Bafq metallogenic province, Central Iran: Evidence from BSE imaging and apatite EPMA and LA-ICP-MS U-Pb geochronology. Minerals 8, 87.

Heimann, A., Beard, B.L., Johnson, C.M., 2008. The role of volatile exsolution and sub-solidus fluid/rock interactions in producing high $^{56}Fe/^{54}Fe$ ratios in siliceous igneous rocks. Geochem. Cosmochim. Acta 72, 4379-4396.

Hemley, J.J., Cygan, G.L., d'Angelo, W.M., 1986. Effect of pressure on ore mineral solubilities under hydrothermal conditions. Geology 14, 377-379.

Hitzman, M.W., 2000. Iron oxide-Cu-Au deposits: What, where, when, and why, in: Porter, T. (Ed.), Hydrothermal Iron Oxide Copper-Gold & Related Deposits: A Global Perspective, 1. PGC Publishing, Adelaide, pp. 9-25.

Hitzman, M.W., Oreskes, N., Einaudi, M.T., 1992. Geological characteristics and tectonic setting of Proterozoic iron oxide (Cu-U-Au-REE) deposits. Precambrian Res. 58, 241-287.

Holwell, D.A., Fiorentini, M., McDonald, I., Lu, Y., Giuliani, A., Smith, D.J., Keith, M. and Locmelis, M., 2019. A metasomatized lithospheric mantle control on the metallogenic signature of post-subduction magmatism. Nature Comm., 10(1), 1-10.

Hu, J., Wang, H., Tan, J., 2020. Fe and C isotopes constrain the pathways of hematite and Fe–rich carbonates formation in the Late Neoproterozoic Dahongliutan BIF, NW China. Ore Geol. Rev. 121, 103485.

Huang, X.-W., Boutroy, É., Makvandi, S., Beaudoin, G., Corriveau, L., De Toni, A.F., 2019. Trace element composition of iron oxides from IOCG and IOA deposits: Relationship to hydrothermal alteration and deposit subtypes. Mineral. Deposita 54, 525-552.

Huang, X.-W., Gao, J.-F., Qi, L., Meng, Y.-M., Wang, Y.-C., Dai, Z.-H., 2016. In-situ LA–ICP–MS trace elements analysis of magnetite: The Fenghuangshan Cu–Fe–Au deposit, Tongling, Eastern China. Ore Geol. Rev. 72, 746-759.

Jackson, S.E., Pearson, N.J., Griffin, W.L., Belousova, E.A., 2004. The application of laser ablation-inductively coupled plasma-mass spectrometry to in situ U-Pb zircon geochronology. Chem. Geol. 211, 47-69.

Johnson, C.A., Day, W.C., Rye, R.O., 2016. Oxygen, hydrogen, sulfur, and carbon isotopes in the Pea Ridge magnetite-apatite deposit, southeast Missouri, and sulfur isotope comparisons to other iron deposits in the region. Econ. Geol. 111, 2017-2032.

Johnson, C.M., Beard, B.L., Beukes, N.J., Klein, C., O'Leary, J.M., 2003. Ancient geochemical cycling in the Earth as inferred from Fe isotope studies of banded iron formations from the Transvaal Craton. Contrib. Mineral. Petrol. 144, 523-547.

Kisvarsanyi, E.B., 1980. Granitic ring complexes and Precambrian hot-spot activity in the St. Francois terrane, Midcontinent region, United States. Geology 8, 43-47.

Kisvarsanyi, E.B., 1981. Geology of the Precambrian St. Francois Terrane, Southeastern Missouri, in: Contribution to Precambrian Geology No. 8. Missouri Department of Natural Resources, Division of Geology and Land Survey, Report of Investigations 64, 58 p.

Kisvarsanyi, E.B., 1984. The Precambrian tectonic framework of Missouri as interpreted from the magnetic anomaly map. In: Contribution to Precambrian Geology No. 14-B. Missouri Department of Natural Resources, Division of Geology and Land Survey, 19 p.

Kisvarsanyi, E.B., 1990. General features of the St. Francois and Spavinaw Granite-Rhyolite terranes and the Precambrian metallogenic region of southeast Missouri, in: Pratt, W.P., Sims, P.K. (Eds.), The Midcontinent of the United States-Permissive Terrane for an Olympic Dam-Type Deposit. U.S. Geological Survey, Denver, CO, Midcontinent Strategic and Critical Minerals Project 1988, Workshop Report, pp. 48-57.

Kisvarsanyi, E.B., Kisvarsanyi, G., 1990. Alkaline granite ring complexes and metallogeny in the Middle Proterozoic St. Francois terrane, southeastern Missouri, USA. Geological Association of Canada Special Paper, 38, pp. 433-446.

Kisvarsanyi, G., Kisvarsanyi, E.B., 1989. Precambrian geology and ore deposits of the Southeast Missouri Iron Metallogenic Province, in: Max Brown, V., Kisvarsanyi, E.B., Hagni, R.D. (Eds.), "Olympic Dam-Type" Deposits and Geology of Middle Proterozoic Rocks in the St. Francois Mountains Terrane, Missouri. Society of Economic Geologists Inc., SEG Guidebook Series, 4, pp. 1-40.

Kisvarsanyi, G., Proctor, P.D., 1967. Trace element content of magnetites and hematites, Southeast Missouri Iron Metallogenic Province, USA. Econ. Geol. 62, 449-471.

Kisvarsanyi, G., Smith, F.J., 1988. Boss-Bixby, a high temperature iron-copper deposit in the Precambrian of the midcontinent United States, in: Open-File Report OFR-88-72-GI. Missouri Department of Natural Resources, Division of Geology and Land Survey,11 p.

Knipping, J.L., Bilenker, L.D., Simon, A.C., Reich, M., Barra, F., Deditius, A.P., Wälle, M., Heinrich, C.A., Holtz, F., Munizaga, R., 2015. Trace elements in magnetite from massive iron oxide-apatite deposits indicate a combined formation by igneous and magmatic-hydrothermal processes. Geochem. Cosmochim. Acta 171, 15-38.

Kreiner, D.C., Barton, M.D., 2017. Sulfur-poor intense acid hydrothermal alteration: A distinctive hydrothermal environment. Ore Geol. Rev. 88, 174-187.

Krneta, S., Ciobanu, C.L., Cook, N.J., Ehrig, K., Kontonikas-Charos, A., 2017. Rare earth element behaviour in apatite from the Olympic Dam Cu–U–Au–Ag deposit, South Australia. Minerals 7, 135.

Locmelis, M., Moroni, M., Denyszyn, S.W., Webb, L.E., Fiorentini, M.L., Sessa, G., Caruso, S., Mathur, R. and Nanzad, B., 2020. On the formation of magmatic sulphide systems in the lower crust by long-lived mass transfer through the lithosphere: Insights from the Valmaggia pipe, Ivrea Verbano Zone, Italy. Terra Nova. 00:1–13.

Loucks, R.R., 2014. Distinctive composition of copper-ore-forming arc magmas. Australian J. Earth Sci. 61, 5-16.

Lowell, G., Rämö, O., 1999. Petrology and geochemistry of the Shepherd Mountain gabbro-implications for basalt genesis at 1.33 Ga in southeast Missouri. Abstr. Programs Geol. Soc. Am. 31 (5), 32.

Lowell, G.R., 2000. Eruptive style of Mesoproterozoic A-type calderas in southeastern Missouri, USA. Rev. Brasi. Geoci. 30, 745-748.

Ludwig, K., 2012. Isoplot/Ex rev. 3.75 - A Geochronological Toolkit for Microspft Excel. Berkeley Geochronology Center. Special Publication, No. 5, 75 p.

Mao, M., Rukhlov, A.S., Rowins, S.M., Spence, J., Coogan, L.A., 2016. Apatite trace element compositions: A robust new tool for mineral exploration. Econ. Geol. 111, 1187-1222.

Maréchal, C.N., Télouk, P., Albarède, F., 1999. Precise analysis of copper and zinc isotopic compositions by plasma-source mass spectrometry. Chem. Geol. 156, 251-273.

Markl, G., von Blanckenburg, F., Wagner, T., 2006. Iron isotope fractionation during hydrothermal ore deposition and alteration. Geochem. Cosmochim. Acta 70, 3011-3030.

McCafferty, A.E., Phillips, J., Driscoll, R.L., 2016. Magnetic and gravity gradiometry framework for Mesoproterozoic iron oxide-apatite and iron oxide-copper-gold deposits, southeast Missouri, USA. Econ. Geol. 111, 1859-1882.

McDonough, W.F., Sun, S.-S., 1995. The composition of the Earth. Chem. Geol. 120, 223-253.

McDowell, F.W., McIntosh, W.C., Farley, K.A., 2005. A precise ^{40}Ar–^{39}Ar reference age for the Durango apatite (U–Th)/He and fission-track dating standard. Chem. Geol. 214, 249-263.

McPhie, J., Kamenetsky, V., Allen, S., Ehrig, K., Agangi, A., Bath, A., 2011. The fluorine link between a supergiant ore deposit and a silicic large igneous province. Geology 39, 1003-1006.

Mendes, M., Lobato, L.M., Kunzmann, M., Halverson, G.P., Rosière, C.A., 2017. Iron isotope and REE+Y composition of the Cauê banded iron formation and related iron ores of the Quadrilátero Ferrífero, Brazil. Mineral. Deposita 52, 159-180.

Menuge, J.F., Brewer, T.S., Seeger, C.M., 2002. Petrogenesis of metaluminous A-type rhyolites from the St. Francois Mountains, Missouri and the Mesoproterozoic evolution of the southern Laurentian margin. Precambrian Res. 113, 269-291.

Mercer, C.N., Watts, K.E., Gross, J., 2020. Apatite trace element geochemistry and cathodoluminescent textures-A comparison between regional magmatism and the Pea Ridge IOAREE and Boss IOCG deposits, southeastern Missouri iron metallogenic province, USA. Ore Geol. Rev. 116, 103129.

Michard, A., 1989. Rare earth element systematics in hydrothermal fluids. Geochem. Cosmochim. Acta 53, 745-750.

Migdisov, A.A., Williams-Jones, A.E., 2014. Hydrothermal transport and deposition of the rare earth elements by fluorine-bearing aqueous liquids. Mineral. Deposita 49, 987-997.

Nadoll, P., Angerer, T., Mauk, J.L., French, D., Walshe, J., 2014. The chemistry of hydrothermal magnetite: A review. Ore Geol. Rev. 61, 1-32.

Nadoll, P., Mauk, J.L., Hayes, T.S., Koenig, A.E., Box, S.E., 2012. Geochemistry of magnetite from hydrothermal ore deposits and host rocks of the Mesoproterozoic Belt Supergroup, United States. Econ. Geol. 107, 1275-1292.

Neymark, L., Holm-Denoma, C.S., Pietruszka, A., Aleinikoff, J.N., Fanning, C.M., Pillers, R.M., Moscati, R.J., 2016a. High spatial resolution U-Pb geochronology and Pb isotope geochemistry of magnetite-apatite ore from the Pea Ridge iron oxide-apatite deposit, St. Francois Mountains, southeast Missouri, USA. Econ. Geol. 111, 1915-1933.

Neymark, L.A., Holm-Denoma, C.S., Pietruszka, A.J., Meighan, C.J., Moscati, R.J., 2016b. In situ LA-ICPMS U-Pb geochronology of apatite from IOA and IOCG deposits, St. Francois Mountains, southeast Missouri, USA. GSA Annual Meeting, Denver, CO.

Nold, J.L., Davidson, P., Dudley, M.A., 2013. The Pilot Knob Magnetite Deposit in the Proterozoic St. Francois Mountains Terrane, southeast Missouri, USA: A magmatic and hydrothermal replacement iron deposit. Ore Geol. Rev. 53, 446-469.

Nold, J.L., Dudley, M.A., Davidson, P., 2014. The Southeast Missouri (USA) Proterozoic iron metallogenic province-Types of deposits and genetic relationships to magnetite–apatite and iron oxide–copper–gold deposits. Ore Geol. Rev. 57, 154-171.

Ondrejka, M., Broska, I., Uher, P., 2015. The late magmatic to subsolidus T-fO2 evolution of the Lower Triassic A- type rhyolites (Silicic Superunit, Western Carpathians, Slovakia): Fe–Ti oxythermometry and petrological implications. Acta Geologica Slovaca 7, 51-61.

Oreskes, N., Einaudi, M.T., 1990. Origin of rare earth element-enriched hematite breccias at the Olympic Dam Cu-U-Au-Ag deposit, Roxby Downs, South Australia. Econ. Geol. 85, 1-28.

Oreskes, N., Einaudi, M.T., 1992. Origin of hydrothermal fluids at Olympic Dam; preliminary results from fluid inclusions and stable isotopes. Econ. Geol. 87, 64-90.

Ovalle, J.T., La Cruz, N.L., Reich, M., Barra, F., Simon, A.C., Konecke, B.A., Rodriguez-Mustafa, M.A., Deditius, A.P., Childress, T.M., Morata, D., 2018. Formation of massive iron deposits linked to explosive volcanic eruptions. Sci. Rep. 8, 14855.

Panno, S., 1978. Structural and volcanic stratigraphy controls on ore emplacement at the Pilot Knob iron ore mine, Iron County, Missouri. Master's thesis, Southern Illinois University, 120 p.

Panno, S.V., Hood, W.C., 1983. Volcanic stratigraphy of the Pilot Knob iron deposits, Iron County, Missouri. Econ. Geol. 78, 972-982.

Pearce, J.A., Harris, N.B.W., Tindle, A.G., 1984. Trace element discrimination diagrams for the tectonic interpretation of granite rocks. J. Petrol. 25, 956-983

Poitrasson, F., Freydier, R., 2005. Heavy iron isotope composition of granites determined by high resolution MC-ICP-MS. Chem. Geol. 222, 132-147.

Pratt, W.P., Anderson, R.E., Berry Jr, A.W., Bickford, M.E., Kisvarsanyi, E.B., Sides, J.R., 1979. Geologic map of exposed Precambrian rocks, Rolla 1° by 2° Quadrangle, Missouri: U.S. Geological Survey, Miscellaneous Investigations Series, I-1161, 1:250,000.

Rapp, J.F., Klemme, S., Butler, I.B., Harley, S.L., 2010. Extremely high solubility of rutile in chloride and fluoride-bearing metamorphic fluids: An experimental investigation. Geology 38, 323-326.

Reid, A., 2019. The Olympic Cu-Au province, Gawler craton: A review of the lithospheric architecture, geodynamic setting, alteration systems, cover successions and prospectivity. Minerals 9, 371.

Rieger, A.A., Marschik, R., Díaz, M., 2012. The evolution of the hydrothermal IOCG system in the Mantoverde district, northern Chile: New evidence from microthermometry and stable isotope geochemistry. Mineral. Deposita 47, 359-369.

Ring, U., Gerdes, A., 2016. Kinematics of the Alpenrhein-Bodensee graben system in the Central Alps: Oligocene/Miocene transtension due to formation of the Western Alps arc. Tectonics 35, 1367-1391.

Rosière, C.A., Rios, F.J., 2006. Specularitic iron ores and shear zones in the Quadrilátero Ferrífero District. App. Earth Sci. 115, 134-138.

Rusk, B.G., Lowers, H.A., Reed, M.H., 2008. Trace elements in hydrothermal quartz: Relationships to cathodoluminescent textures and insights into vein formation. Geology 36, 547-550.

Ryan, R.F., 1981. The Pilot Knob Hematite Deposit. In: Kisvarsanyi, E.B., Hebrank, A.W., Ryan, R.F. (Eds.), Guidebook to the geology and ore deposits of the St. Francois Mountains, Missouri. Missouri Department of Natural Resources, Division of Geology and Land Survey, Report of Investigation, 67, pp. 111-114.

Schlegel, T.U., Wagner, T., Wälle, M., Heinrich, C.A., 2018. Hematite breccia-hosted iron oxide copper-gold deposits require magmatic fluid components exposed to atmospheric oxidation: Evidence from Prominent Hill, Gawler Craton, South Australia. Econ. Geol. 113, 597-644.

Schoene, B., Bowring, S.A., 2006. U–Pb systematics of the McClure Mountain syenite: thermochronological constraints on the age of the $^{40}Ar/^{39}Ar$ standard MMhb. Contrib. Mineral. Petrol. 151, 615.

Seeger, C., 2000. Southeast Missouri iron metallogenic province: Characteristics and general chemistry. In: Porter, T.M. (Ed.), Hydrothermal Iron Oxide Copper-Gold & Related Deposits: A Global Perspective ,1. PGC Publishing, Adelaide, pp. 237-248.

Seeger, C.M., 2003. Lithology and alteration assemblages of the Boss iron-copper deposit, Iron and Dent Counties, Southeast Missouri. Ph.D. dissertation, University of Missouri-Rolla, Rolla, MO, 139 p.

Seeger, C.M., Marikos, M.A., Nuelle, L.M., 1989. The Pilot Knob Hematite deposit (Field trip stop No. 2). In: Max Brown, V., Kisvarsanyl, E.B., Hagni, R.D. (Eds.), "Olympic Dam-Type" Deposits and Geology of Middle Proterozoic Rocks in the St. Francois Mountains Terrane, Missouri. Society of Economic Geologists Inc., SEG Guidebook Series, 4, pp. 55-68.

1240 Sidder, G.B., Day, W.C., Nuelle, L.M., Seeger, C.M., Kisvarsanyi, E.B., 1993. Mineralogic and
1241 fluid-inclusion studies of the Pea Ridge iron-rare-earth-element deposit, Southeast
1242 Missouri. U.S. Geol. Surv. Bull 2039, 205-216.
1243 Sides, J.R., Bickford, M.E., Shuster, R.D., Nusbaum, R.L., 1981. Calderas in the Precambrian
1244 terrane of the St. Francois Mountains, southeastern Missouri. J. Geophys. Res. 86, 10349-
1245 10364.
1246 Simon, A.C., Knipping, J., Reich, M., Barra, F., Deditius, A.P., Bilenker, L., Childress, T., 2018.
1247 Kiruna-type iron oxide-apatite (IOA) and iron oxide copper-gold (IOCG) deposits form
1248 by a combination of igneous and magmatic-hydrothermal processes: Evidence from the
1249 Chilean Iron Belt. In: Arribas, A.M., Mauk, J.L. (Eds.), Metals, Minerals, and Society.
1250 Society of Economic Geologists, Inc., SEG Special Publications, 21, pp. 89-114.
1251 Sims, P., Petermar, Z., 1986. Early Proterozoic Central Plains orogen: A major buried structure
1252 in the north-central United States. Geology 14, 488-491.
1253 Skirrow, R.G., 2010. "Hematite-group" IOCG-U systems: Tectonic settings, hydrothermal
1254 characteristics, and Cu-Au and U mineralizing processes. In: Corriveau, L., Mumin, A.H.
1255 (Eds.), Exploring for Iron Oxide Copper-Gold Deposits: Canada and Global Analogues.
1256 Geological Association of Canada, Short Course Notes, 20, pp. 39-58.
1257 Stacey, J.S., Kramers, J.D., 1975. Approximation of terrestrial lead isotope evolution by a two-
1258 stage model. Earth Planet. Sci. Lett. 26, 207-221.
1259 Stallings, M.D., Hagni, R., Seeger, C., 2001. Mineralogy and petrology of the Bourbon
1260 Precambrian iron deposit of southeastern Missouri, and its comparison to the Olympic
1261 Dam-type deposits of South Australia. Abstr. Programs Geol. Soc. Am. 33 (7), 19.
1262 Starkey, M.A., Seeger, C.M., 2016. Mining and exploration history of the Southeast Missouri
1263 Iron Metallogenic Province. Econ. Geol. 111, 1815-1823.
1264 Sun, J., Zhu, X., Chen, Y., Fang, N., 2013. Iron isotopic constraints on the genesis of Bayan Obo
1265 ore deposit, Inner Mongolia, China. Precambrian Res. 235, 88-106.
1266 Sverjensky, D.A., 1984. Europium redox equilibria in aqueous solution. Earth Planet. Sci. Lett.
1267 67, 70-78.
1268 Tanis, E.A., Simon, A., Zhang, Y., Chow, P., Xiao, Y., Hanchar, J.M., Tschauner, O., Shen, G.,
1269 2016. Rutile solubility in NaF–NaCl–KCl-bearing aqueous fluids at 0.5–2.79 GPa and
1270 250–650°C. Geochem. Cosmochim. Acta 177, 170-181.
1271 Taylor, P.D.P., Maeck, R., De Bièvre, P., 1992. Determination of the absolute isotopic
1272 composition and atomic weight of a reference sample of natural iron. Int. J. Mass.
1273 Spectrom. Ion Proces. 121, 111-125.
1274 Thomas, W.A., Tucker, R.D., Astini, R.A., Denison, R.E., 2012. Ages of pre-rift basement and
1275 synrift rocks along the conjugate rift and transform margins of the Argentine
1276 Precordillera and Laurentia. Geosphere 8, 1366-1383.
1277 Thomson, S.N., Gehrels, G.E., Ruiz, J., Buchwaldt, R., 2012. Routine low-damage apatite U-Pb
1278 dating using laser ablation–multicollector–ICPMS. Geochem. Geophys. Geosystems 13.
1279 Troll, V.R., Weis, F.A., Jonsson, E., Andersson, U.B., Majidi, S.A., Högdahl, K., Harris, C.,
1280 Millet, M.-A., Chinnasamy, S.S., Kooijman, E., Nilsson, K.P., 2019. Global Fe–O
1281 isotope correlation reveals magmatic origin of Kiruna-type apatite-iron-oxide ores.
1282 Nature Communications 10, 1712.
1283 Tropper, P., Manning, C.E., 2005. Very low solubility of rutile in H_2O at high pressure and
1284 temperature, and its implications for Ti mobility in subduction zones. Am. Mineral. 90,
1285 502-505.

Van Schmus, W., Bickford, M., Turek, A., Van der Pluijm, B., Catacosinos, P., 1996. Proterozoic geology of the east-central Midcontinent basement. Geological Society of America Special Papers, pp. 7-32.

Verdugo-Ihl, M.R., Ciobanu, C.L., Cook, N.J., Ehrig, K.J., Courtney-Davies, L., Gilbert, S., 2017. Textures and U-W-Sn-Mo signatures in hematite from the Olympic Dam Cu-U-Au-Ag deposit, South Australia: Defining the archetype for IOCG deposits. Ore Geol. Rev. 91, 173-195.

Vermeesch, P., 2018. IsoplotR: A free and open toolbox for geochronology. Geosci. Front. 9, 1479-1493.

Walker, J.A., Pippin, C.G., Cameron, B.I., Patino, L., 2002. Tectonic insights provided by Mesoproterozoic mafic rocks of the St. Francois Mountains, southeastern Missouri. Precambrian Res. 117, 251-268.

Watts, K.E., Mercer, C.N., 2020. Zircon-hosted melt inclusion record of silicic magmatism in the Mesoproterozoic St. Francois Mountains terrane, Missouri: Origin of the Pea Ridge iron oxide-apatite-rare earth element deposit and implications for regional crustal pathways of mineralization. Geochem. Cosmochim. Acta 272, 54-77.

Weis, F., 2013. Oxygen and iron isotope systematics of the Grängesberg mining district (GMD), central Sweden. Ph.D. dissertation, Uppsala University, 83 p.

Wen, G., Li, J.-W., Hofstra, A.H., Koenig, A.E., Lowers, H.A., Adams, D., 2017. Hydrothermal reequilibration of igneous magnetite in altered granitic plutons and its implications for magnetite classification schemes: Insights from the Handan-Xingtai iron district, North China Craton. Geochem. Cosmochim. Acta 213, 255-270.

Whalen, J.B., Currie, K.L., Chappell, B.W., 1987. A-type granites: geochemical characteristics, discrimination and petrogenesis. Contrib. Mineral. Petrol. 95, 407-419.

Williams, P.J., Barton, M.D., Johnson, D.A., Fontboté, L., De Haller, A., Mark, G., Oliver, N.H., Marschik, R., 2005. Iron oxide copper-gold deposits: Geology, space-time distribution, and possible modes of origin. Econ. Geol. 100th Anniversary Volume, 371-405.

Winchester, J.A., Floyd, P.A., 1977. Geochemical discrimination of different magma series and their differentiation products using immobile elements. Chem. Geol. 20, 325-343.

Wracher, D.A., 1976. Geology of the Pilot Knob Magnetite Deposit, Southeast Missouri. In: Kisvarsanyi, E.B. (Ed.), Studies in Precambrian geology of Missouri. Missouri Department of Natural Resources, Division of Geology and Land Survey, Report of Investigations, 61, pp. 155-163.

Yesavage, T., Stinchcomb, G.E., Fantle, M.S., Sak, P.B., Kasznel, A., Brantley, S.L., 2016. Investigation of a diabase-derived regolith profile from Pennsylvania: Mineralogy, chemistry and Fe isotope fractionation. Geoderma 273, 83-97.

Highlights

- The Pilot Knob Magnetite (PKM) and overlying hematite (PKH) deposit were studied

1328 - The mineralization age of the Pilot Knob Magnetite (PKM) deposit is 1437.7±5.8 Ma
1329 - The surface-near Pilot Knob Hematite (PKH) deposit formed from hydrothermal fluids
1330 - The PKM and PKH deposits are endmembers of a magmatic-hydrothermal continuum
1331 - The deposits formed during transition from a convergent to extensional regime

1332